nature cardiovascular research

Article

https://doi.org/10.1038/s44161-026-00818-2

CAMK2D causes heart failure in mice with RBM20 cardiomyopathy

Received: 23 May 2025

Accepted: 15 April 2026

Published online: 04 May 2026

Check for updates

Maarten M. G. van den Hoogenhof[1,2,3,4] ✉, Javier Duran[1,2,3,5], Thiago Britto-Borges[3,6], Vasco Sequeira[7], Elena Kemmling[1,2,4], Laura Konrad[1,2], Friederike Schreiter[1,2,3], David C. Lennermann[1,2], Joshua Hartmann[1,2], Laura Schraft[3,8], Julia Kornienko[3,8], Theresa Bock[9], Marcus Krüger[9], Christoph Maack[7], Christoph Dieterich[1,3,6], Lars M. Steinmetz[3,8,10], Matthias Dewenter[1,2,3] & Johannes Backs[1,2,3,4,5] ✉

Although heart disease arises from different etiologies, treatment remains largely one-size-fits-all, leaving many patients without optimal benefit, which highlights the need for cause-directed therapies. Pathogenic variants in *RBM20*, a cardiac splicing factor, lead to an aggressive form of dilated cardiomyopathy with high risk of ventricular arrhythmias. We hypothesized that the splicing target calcium/calmodulin-dependent kinase II delta (*CAMK2D*) is disease causing in RBM20 cardiomyopathy. Here we show that *Rbm20/Camk2d* double knockout mice are protected from heart failure and sudden cardiac death. In *Rbm20*-deficient hearts, phosphorylation of CAMK2D targets was increased, indicating that RBM20 loss results not only in mis-splicing of *Camk2d* transcripts but also in functional activation of CAMK2D signaling. Reexpression of individual CAMK2D splice variants in *Rbm20/Camk2d* double knockout mice reintroduced cardiac dysfunction, demonstrating that overactivation, rather than mis-splicing, drives disease. Treatment of *Rbm20*-p.Arg636Gln knockin mice with the ATP-competitive CAMK2 inhibitor hesperadin improved cardiac function. These findings identify CAMK2D overactivation as a central mechanism in RBM20 cardiomyopathy and support CAMK2D inhibition as a promising cause-directed therapy.

Heart disease is the most frequent cause of death and is often caused by dilated cardiomyopathy (DCM)[1]. DCM is defined by left ventricular or biventricular systolic dysfunction and dilation that are not explained by abnormal loading conditions or coronary artery disease[2]. The prevalence of DCM is approximately 1:250, of which ~30–50% of cases are familial[3–5]. Pathogenic variants that are causal for familial DCM can be found in a variety of genes, including *RBM20*, which accounts for approximately 3% of familial DCM cases[3]. Despite specific etiologies, there is currently no cause-directed DCM therapy. In stark contrast, the development of tailored therapies in oncology has revolutionized the clinical care of patients with cancer[6]. In the cardiac field, the development of mavacamten for obstructive hypertrophic cardiomyopathy (oHCM) has demonstrated that the treatment of the specific underlying pathophysiology can also improve the outcome of patients with cardiovascular disease[7]. RBM20, or RNA binding motif protein 20, is a cardiac-enriched splice factor. Pathogenic *RBM20* variants lead to a severe form of DCM characterized by an early onset of disease and a high burden of malignant arrhythmias causing sudden cardiac death, which is generally termed RBM20 cardiomyopathy[8]. RBM20 is involved in proper splicing of a multitude of cardiac genes, including *TTN*, *RYR2*,

A full list of affiliations appears at the end of the paper. ✉e-mail: maarten.hoogenhof@cardioscience.uni-heidelberg.de; johannes.backs@cardioscience.uni-heidelberg.de

CAMK2D and *LDB3* (refs. 9,10). Loss of functional RBM20 generally leads to inclusion of exons, and RBM20 is therefore regarded as a splicing repressor[11]. Many studies on RBM20 have focused on TTN, which is mis-spliced into a giant and heavily compliant isoform, due to the inclusion of exons between exon 50 and 219, termed N2BA-Giant[10,11]. It has been hypothesized and shown that an increase in this isoform through downregulation of RBM20 might be beneficial, especially in the setting of diastolic dysfunction[12,13]. However, an increase in this TTN isoform could potentially impact and decrease systolic function. Another direct target of RBM20 is the multifunctional *CAMK2D*. In the heart, CAMK2D is known to have at least 11 different splice isoforms, of which CAMK2D-9 is the most expressed isoform in the human heart[14]. The different splice isoforms of CAMK2D have overlapping, but also distinct, functions that are currently not completely unraveled[15]. Increased activation of CAMK2D contributes to a variety of pathological cardiac conditions, including ischemic heart disease and pressure-overload-induced heart failure, as it is seen in chronic arterial hypertension[16]. However, it is unknown whether a specific splice variant or several variants are mainly responsible for these detrimental effects. CAMK2D works in heteromultimers, and can include different splice isoforms in different ratios. It is hypothesized that the ratio of these splice isoforms determines the preference of the enzyme for localization in different cellular compartments or for the phosphorylation of different proteins[17]. For example, CAMK2D-B is mostly nuclear and is known for its involvement in transcription regulation[18,19], while CAMK2D-C is mostly cytoplasmic and is known for its involvement in calcium handling and mitochondrial regulation[20,21]. In RBM20 cardiomyopathy, CAMK2D is mis-spliced and activated, but its contribution to the molecular mechanisms that underlie RBM20 cardiomyopathy is unknown. Furthermore, recent findings suggest that the clinical phenotype of RBM20 cardiomyopathy is not solely caused by a loss of splicing, but that pathogenic variants in the RS region of *RBM20* lead to cytoplasmic ribonucleoprotein granule formation, which is an additional detrimental mechanism[22,23]. Specifically, variants in the RS domain (especially in the RSRSP stretch) of *RBM20* disrupt its interaction with the nuclear import receptor TNPO3, resulting in mislocalization and cytoplasmic retention[24]. This mechanism is supported by the observation that pig, mouse and human induced pluripotent stem (hiPS) cells with variants in the RS region of *RBM20* have a more severe phenotype than *Rbm20* knockout (KO) models, highlighting the pathological significance of RBM20 mislocalization alongside its splicing dysfunction[22,23,25,26]. Here, we hypothesized that CAMK2D is a critical target of RBM20, and generated *Rbm20*/*Camk2d* double knockout (DKO) mice. We characterized these mice functionally and molecularly, and showed that DKO mice have similar splicing abnormalities in RBM20 targets, but were protected against cardiac dysfunction and lethal arrhythmias. We further show that this effect is dependent on CAMK2D overactivation, but independent on splice isoform expression. Lastly, we show in a recently established mouse model of RBM20 cardiomyopathy, carrying a pathogenic variant in the RS domain and characterized by cytoplasmic ribonucleoprotein granule formation, that pharmacological CAMK2D inhibition reverses heart failure. These data open the door to a cause-directed therapy for patients with DCM due to pathogenic *RBM20* variants.

Results

CAMK2D is mis-spliced in RBM20 cardiomyopathy

We hypothesized that *CAMK2D* might be a critical target of RBM20; therefore, we characterized *CAMK2D* splicing in more detail in multiple models of RBM20 cardiomyopathy. We used existing RNA-sequencing (RNA-seq) datasets from mouse models of RBM20 cardiomyopathy[27,28], as well as hiPS cell-derived cardiomyocytes with disease-causing variants in the *RBM20* gene[29]. We first used *Rbm20* KO mice, identified splice junction reads that were specific to the different cardiac *CAMK2D* splice variants *CAMK2D-A*, *CAMK2D-B*, *CAMK2D-C*, *CAMK2D-4* and *CAMK2D-9*, and corrected them for total expression of *CAMK2D* (exon composition of the different splice variants is depicted in Fig. 1a). We found that in wild-type (WT) mouse hearts *CAMK2D-9* was the most prevalent isoform, followed by *CAMK2D-C* and *CAMK2D-B*, which is in line with recent insights, and loss of RBM20 led to an almost complete switch to *CAMK2D-A* and an increase in *CAMK2D-4* (ref. 14) (Fig. 1b). Two mouse models with a pathogenic variant in *Rbm20* (p.Pro635Leu and p.Arg636Gln) showed similar mis-splicing of CAMK2D (Fig. 1c). We then investigated *CAMK2D* splicing in publicly available RNA-seq data from a human model of RBM20 cardiomyopathy, namely hiPS cells with the p.Pro633Leu and p.Arg634Gln variants in *RBM20* (ref. 29). Interestingly, we similarly observed mis-splicing of *CAMK2D*, but the isoforms expressed were different. In mice, *CAMK2D-A* and *CAMK2D-4* were increased, but in humans we observed an increase in *CAMK2D-9* (Fig. 1d). This difference is due to the lack of expression of exon 15 in humans, which is included in *CAMK2D-A* and *CAMK2D-4*, but not in *CAMK2D-9* (refs. 10,30). Overall, these data show that loss of functional RBM20 leads to mis-splicing of *CAMK2D*, albeit with differences between species.

Rbm20/*Camk2d* DKO mice are protected against cardiac dysfunction

To investigate the contribution of the RBM20 splicing target *CAMK2D* to RBM20 cardiomyopathy, we generated homozygous *Rbm20*/*Camk2d* DKO mice. Histochemistry showed enlarged atria upon loss of RBM20 in *Rbm20* KO and to a lesser extent in DKO, but no other observable morphological changes (Fig. 2a). *Rbm20* expression was abolished in both the *Rbm20* KO and the DKO mice (Fig. 2b). CAMK2D protein was absent from the hearts of *Camk2d* KO and DKO mice (Fig. 2c). Next, we performed cardiac echocardiography and found that *Rbm20* KO mice presented with decreased cardiac function, while DKO mice were protected against cardiac dysfunction (Fig. 2d,e, Extended Data Figs. 1 and 2 and Supplementary Table 1). Additionally, The E/e′ ratio was increased in *Rbm20* KO mice, and similarly prevented in DKO mice (Fig. 2f and Extended Data Fig. 1). We observed no differences between sexes, in line with our previous results in mouse models of RBM20 cardiomyopathy[28] (Extended Data Fig. 1). Atrial size, as measured by echocardiography, was enlarged in *Rbm20* KO mice, while this enlargement was blunted in the DKO mice (Extended Data Fig. 3), supporting the histochemistry data (Fig. 2a). Pressure–volume loop analysis showed an increased ventricular compliance, indicated by a decreased EDPVR (that is a downward/rightward shift of the curve), in *Rbm20* KO and DKO mouse hearts (Extended Data Fig. 3). This may be due to the mis-splicing of TTN, which leads to a much more compliant TTN isoform. This decrease in EDPVR has been observed in other models with loss of RBM20 as well[12]. In line with this, we observed decreased passive force development in single isolated skinned *Rbm20* KO and DKO cardiomyocytes (Extended Data Fig. 3). To evaluate systolic performance, we analyzed end-systolic pressure–volume relationship slope together with preload-recruitable stroke work, which reflects the Frank–Starling mechanism and is relatively independent of load and size. We found that *Rbm20* KO mouse hearts were less contractile, whereas this impairment was attenuated in the DKO hearts (Extended Data Fig. 3). These pressure–volume loop-derived changes in contractility were confirmed at the single-cell level; the tension–Ca^{2+} relationship in isolated skinned cardiomyocytes showed decreased force development in *Rbm20* KO cardiomyocytes, but not in DKO cardiomyocytes, especially at the sarcomere lengths of 1.8 µm (which in mice in vivo lies within the physiological operating range of ~1.90 µm in diastole to ~1.68 µm in systole[31]; Extended Data Fig. 3). Taken together, these data indicate that decreased contractility of the ventricle in *Rbm20* KO hearts is rescued by loss of CAMK2D, while the increased ventricular compliance remains. The increased E/e′ ratio may be due to the ventricular and atrial dilation and regurgitation, and thus not reflecting diminished compliance. The increased running distance in the exercise tolerance test of *Camk2d* KO and DKO, while we found no decrease in the *Rbm20*

https://doi.org/10.1038/s44161-026-00818-2

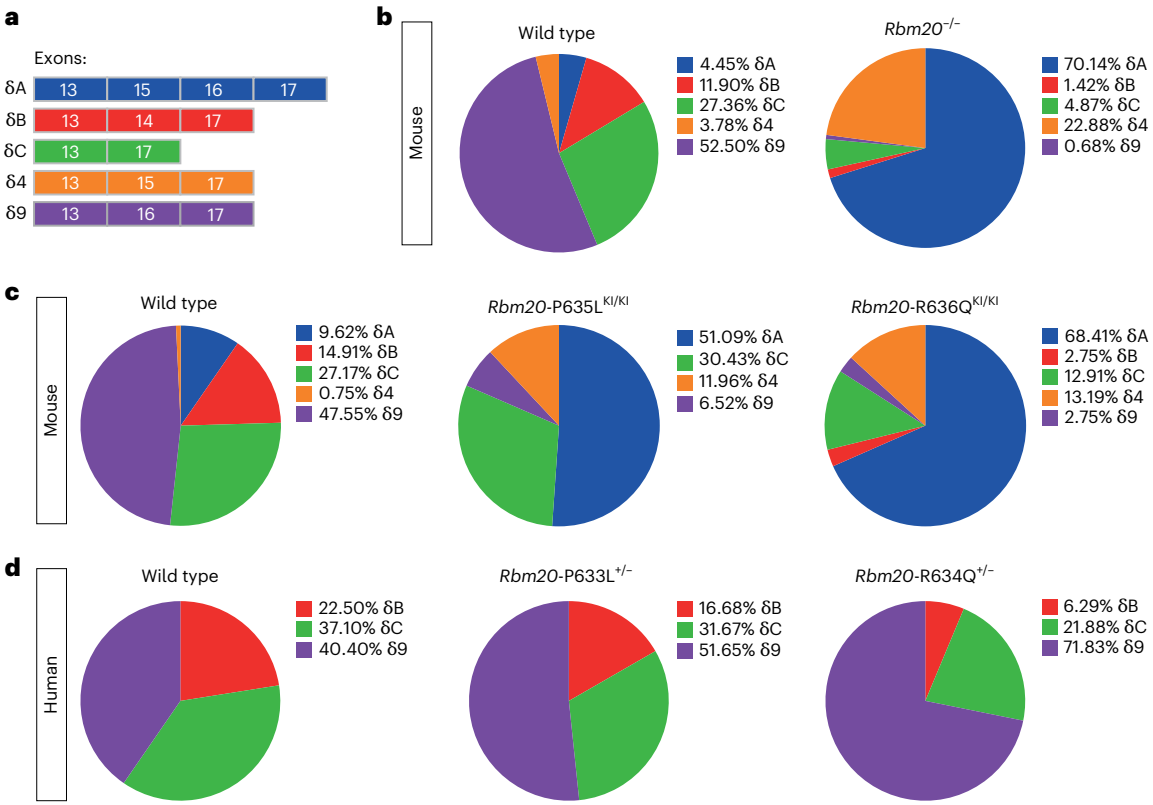

Fig. 1 | *Camk2d* is mis-spliced after loss of functional RBM20. a, Overview of exons 13–17 that are included in the different *Camk2d* splice variants. **b**, Pie charts of the cardiac *Camk2d* splice variants in WT and *Rbm20* KO mouse hearts. **c**, Pie charts of the cardiac *Camk2d* splice variants in WT, *Rbm20*-p.Pro635Leu and *Rbm20*-p.Arg636Gln KI mouse hearts. **d**, Pie charts of the cardiac *CAMK2D* splice variants in WT, *RBM20*-p.Pro633Leu and *RBM20*-p.Arg634Gln mutant hiPS cell-derived cardiomyocytes.

KO, further supports that the cardiac phenotype of *Rbm20* KO mice is not diastolic but rather systolic dysfunction, which is rescued by an increased contractility of the DKO mouse hearts (Extended Data Fig. 3).

To investigate susceptibility to lethal cardiac arrhythmias, we induced arrhythmias by injection of epinephrine and caffeine, and found that while ~71% of *Rbm20* KO mice died within 24 h, only 37.5% of DKO mice died, indicating that DKO mice were partially protected against sudden cardiac death after arrhythmia induction (Fig. 2g). We then investigated known RBM20 splicing targets, and found that *Ttn*, *Ldb3*, *Ryr2* and *Camk2g* were similarly mis-spliced in DKO as in *Rbm20* KO mouse hearts (Fig. 2h). With regards to *Camk2d*, we observed similar mis-splicing on the transcript level, although protein was completely absent from the DKO hearts, which is due to a second transcriptional start site in exon 8 that does not result in a protein[32] (Fig. 2c,h). Interestingly, apart from mis-splicing of *Camk2d*, we also observed an increase in total CAMK2D protein, which correlates with increased CAMK2D activity (Fig. 2c). Phosphoproteomics on the hearts of WT, *Rbm20* KO, *Camk2d* KO and DKO mice revealed increased phosphorylation of 136 protein residues in *Rbm20* KO hearts, of which 27 were normalized in DKO hearts (Fig. 2i and Extended Data Fig. 4). Of these 27 residues, 9 were known or predicted targets of CAMK2, including PLN-T17 and PRKAR1A-S77. This suggests that CAMK2 activity is increased in the hearts of *Rbm20* KO hearts, and this is alleviated in the hearts of DKO mice. Even though CAMK2 activity has been implicated in many forms of cardiac dysfunction, we explored whether CAMK2 activation is a universal hallmark of heart disease, and investigated CAMK2 activity in a new mouse model with the human DCM-causing *LMNA*-p.Lys117fs variant, where we did not observe increased CAMK2 activity (Extended Data Fig. 5). Bulk RNA-seq on the hearts of WT, *Rbm20* KO, *Camk2d* KO and DKO mice revealed a subset of genes (cluster 2) that reverted back to normal levels (Extended Data Fig. 6). Overall, these data show that *Rbm20* KO mice present with cardiac dysfunction and increased susceptibility to sudden cardiac death, which is alleviated by genetic deletion of *Camk2d*.

Reexpression of single *Camk2d* splice variants in DKO mice reintroduces cardiac dysfunction

To investigate which cardiac splice variant(s) of *Camk2d* are required for the cardiomyopathic phenotype in RBM20 cardiomyopathy, we used AAV9-mediated overexpression of the cardiac *Camk2d* splice variants *CAMK2D-A*, *CAMK2D-B*, *CAMK2D-C*, *CAMK2D-4* and *CAMK2D-9* (depicted as δA, δB, δC, δ4 and δ9, respectively) in the hearts of DKO mice. We aimed to reexpress the different splice variants to similar levels as those seen in *Rbm20* KO mice. We injected mice with 2×10^{12} viral genomes of adeno-associated virus serotype 9 (AAV9) encoding N-terminal flag-tagged splice variants of *Camk2d*, performed echocardiography and dissected the organs 4 weeks later (Fig. 3a). Immunoblotting revealed specific expression of flag-tagged CAMK2D in the AAV9-injected mice, and that CAMK2D expression was restored to physiological levels in the AAV9-injected mice (Fig. 3b,c). Cardiac function was impaired in *Rbm20* KO mice, and DKO mice injected with the control AAV9-Luciferase were, as expected, protected against cardiac dysfunction (Fig. 3d). Interestingly, cardiac function was markedly reduced in all DKO mice with reexpression of a *Camk2d* splice variant, regardless of which splice variant was reintroduced (Fig. 3d). Since this suggests that there is at least a partial overlap in function between the different splice isoforms, we investigated cellular localization of the different CAMK2D splice isoforms in vivo by doing cellular fractionation of WT and *Rbm20* KO hearts. Surprisingly, even though *Camk2d* isoform expression is markedly different between WT and *Rbm20* KO mice,

https://doi.org/10.1038/s44161-026-00818-2

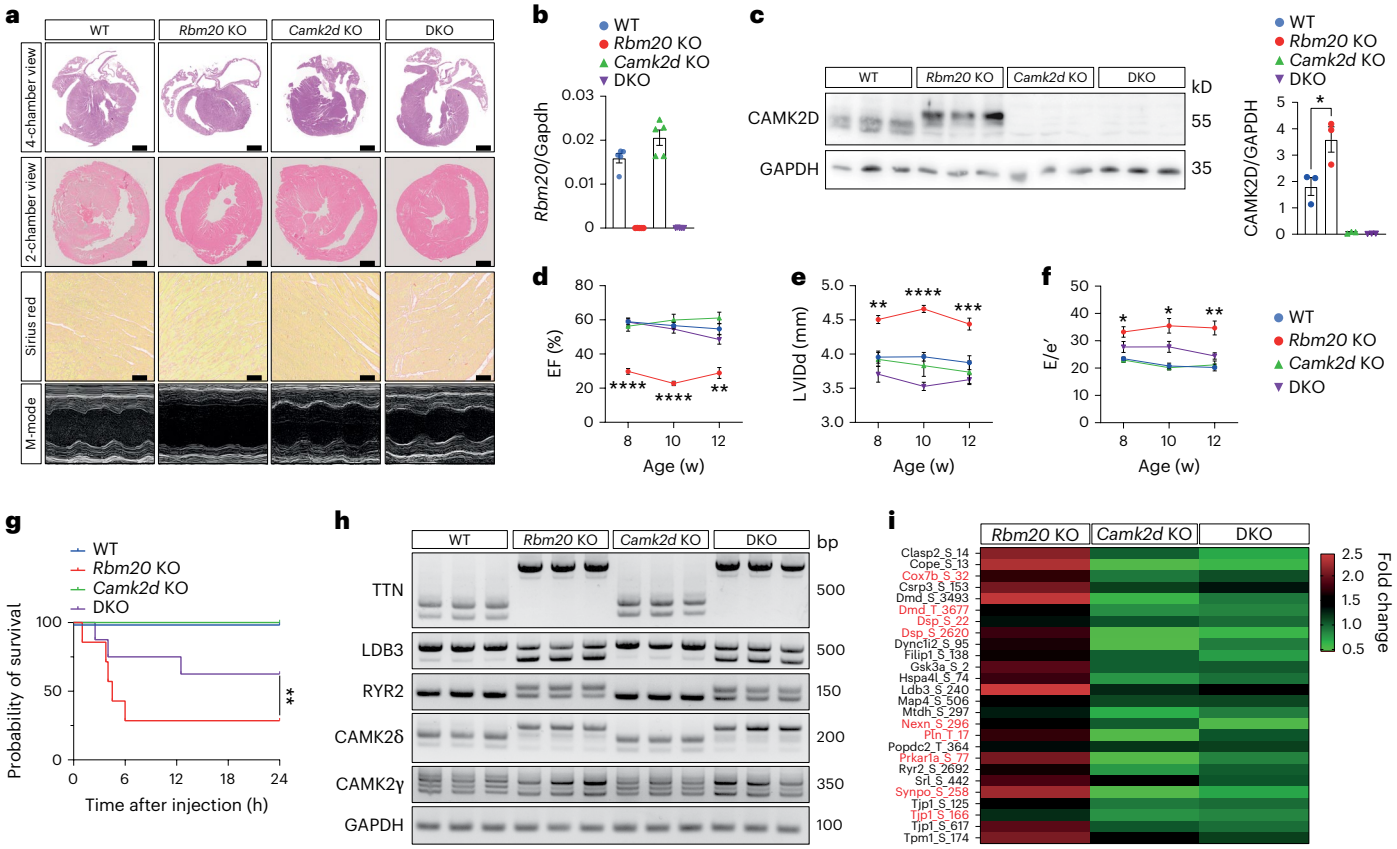

Fig. 2 | *Rbm20*/*Camk2d* DKO mice are protected from cardiac dysfunction and sudden cardiac death. a, Hematoxylin and eosin (H&E) and picrosirius red staining of hearts of WT, *Rbm20* KO, *Camk2d* KO and *Rbm20*/*Camk2d* DKO mice. Scale bars, 1 mm (four-chamber view), 0.75 mm (two-chamber view), 100 µm (picrosirius red). **b**, qPCR of *Rbm20* ($n = 5$ biological replicates). **c**, Western blotting of CAMK2D in left ventricular tissue with quantification ($n = 3$ biological replicates). Significance was tested using a one-way analysis of variance (ANOVA) with Tukey's multiple comparisons test. $^{*}P < 0.05$. **d**–**f**, Cardiac function measured by echocardiography ($n = 8$ biological replicates): ejection fraction (EF; **d**), left ventricular diameter at diastole (LVIDd; **e**) and E/e' (**f**). Significance was tested using one-way ANOVA with Tukey's multiple comparisons test. *Rbm20* KO versus DKO: $^{*}P < 0.05$, $^{**}P < 0.01$, $^{***}P < 0.001$, $^{****}P < 0.0001$. **g**, Survival after arrhythmia induction ($n = 7$ biological replicates for WT and *Rbm20* KO, $n = 5$ biological replicates for *Camk2d* KO and $n = 8$ biological replicates for DKO). Significance was tested using a log-rank (Mantel–Cox) test, P value = 0.007. **h**, PCR with reverse transcription (RT–PCR) of RBM20 splicing targets. Representative gels from three independent experiments. **i**, Heat map of differentially phosphorylated proteins that are increased in the *Rbm20* KO and normalized in the DKO. Proteins in red are known or predicted CAMK2 phosphorylation targets. Data in graphs are presented as mean values ± s.e.m.

we found almost all CAMK2D in the nuclear fraction of both groups, regardless of which isoform was expressed (Extended Data Fig. 7). This suggests that the shift in CAMK2D splice isoform expression has only a limited effect on localization, and potentially function, of the enzyme, at least when ectopically expressed in vivo. Expression of the cardiac stress markers *Anf* and *Bnp* (*Nppa* and *Nppb*) was increased in the hearts of all mice, except WT, and we did not observe any morphological differences between the groups (Fig. 3e and Extended Data Fig. 8). Overall, these results show that reexpression of CAMK2D in DKO mouse hearts is sufficient to reintroduce cardiac dysfunction, regardless of which splice variant is reintroduced. Moreover, this suggests that (over)activation of CAMK2D, and not mis-splicing, underlies the disease phenotype in *Rbm20* KO mice.

Hesperadin treatment ameliorates cardiac dysfunction in *Rbm20*-p.Arg636Gln KI mice

To evaluate the therapeutic potential of CAMK2D inhibition in RBM20 cardiomyopathy, we used hesperadin (not to be confused with hesperidin), an ATP-competitive CAMK2 inhibitor, in *Rbm20*-p.Arg636Gln knockin (KI) mice, which harbor a human disease-causing *Rbm20* variant that leads to cytoplasmic granule formation[33]. We treated heterozygous *Rbm20*-p.Arg636Gln KI mice for 4 weeks with either vehicle (dimethylsulfoxide or DMSO) or hesperadin (2.5 µg or 5 µg per kg body weight[33]; Fig. 4a). At 8 weeks old, heterozygous *Rbm20*-p.Arg636Gln KI mice presented with decreased cardiac function and increased diastolic volume as compared to WT mice (Fig. 4b). Hesperadin treatment completely restored cardiac function, both at 2 weeks and at 4 weeks after the beginning of treatment. In addition, we observed a trend in reduced diastolic volume in the *Rbm20*-p.Arg636Gln KI mouse hearts after treatment, suggesting beneficial effects on structural remodeling (Fig. 4b). Histochemistry revealed no gross morphological changes between vehicle-treated and hesperadin-treated mice (Fig. 4c). *Rbm20* mRNA expression nor RBM20 protein expression or expression of RBM20 targets was affected by hesperadin treatment (Fig. 4d and Extended Data Fig. 9). Furthermore, we used immunohistochemistry to investigate whether hesperadin treatment affected cytoplasmic granule formation, but granule formation was unaffected, pointing to a process downstream of cytoplasmic granule formation that leads to CAMK2D overactivation (Fig. 4e).

Hesperadin treatment inhibits CAMK2D activity in *Rbm20*-p.Arg636Gln KI mice

We then performed RNA-seq on the hearts of these mice to investigate whether hesperadin treatment affected gene expression. We found similar numbers of differentially expressed genes (DEGs) in heterozygous *Rbm20*-p.Arg636Gln KI mice treated with vehicle and with the

https://doi.org/10.1038/s44161-026-00818-2

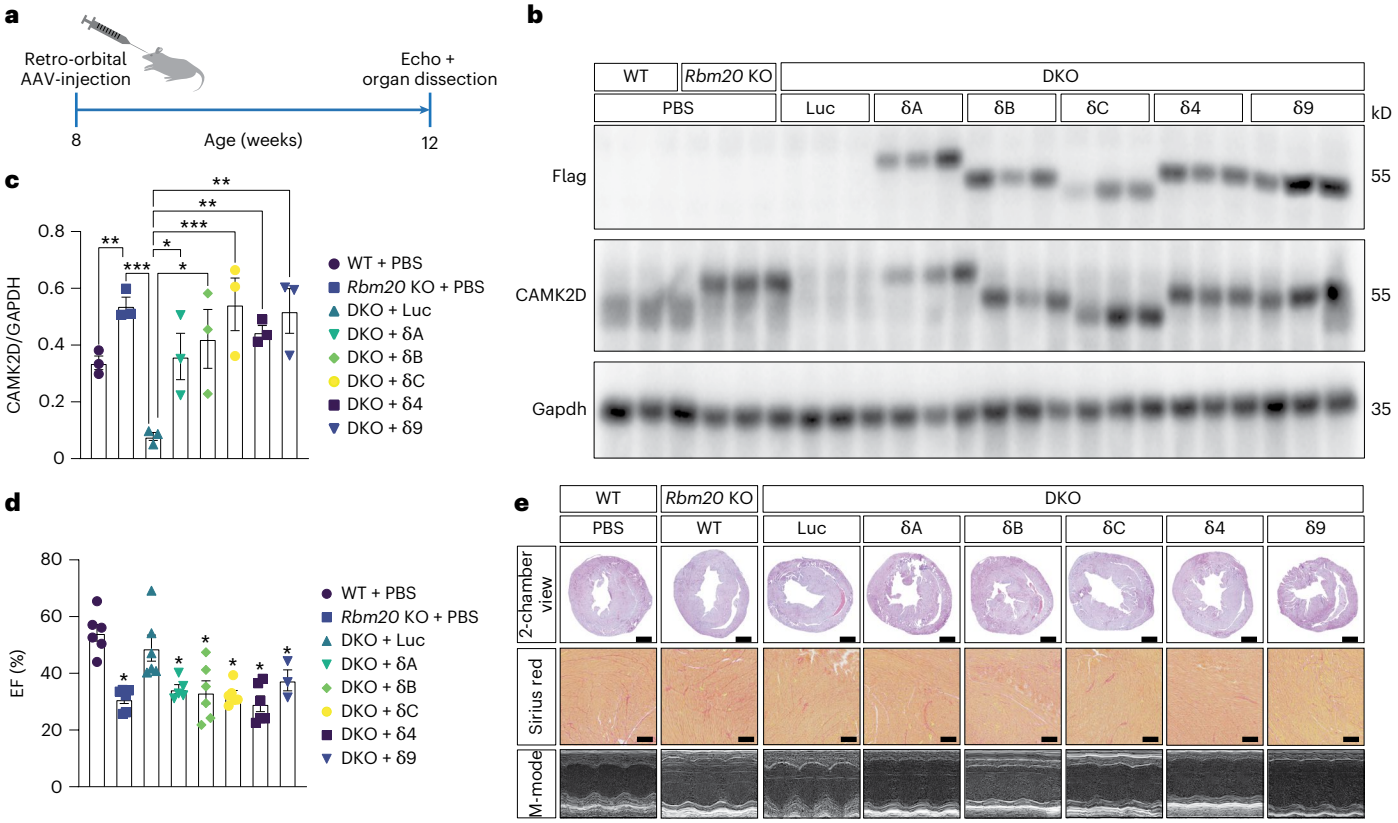

Fig. 3 | Reexpression of CAMK2D splice variants reintroduces cardiac dysfunction in *Rbm20/Camk2d* DKO mice. a, Experimental setup. **b**, Western blotting of CAMK2D and Flag in left ventricular tissue. **c**, Quantification of western blots in **b** ($n = 3$ biological replicates). Significance was tested using one-way ANOVA with Tukey's multiple comparisons test. *Rbm20* KO versus DKO: $^{*}P < 0.05$, $^{**}P < 0.01$, $^{***}P < 0.001$. **d**, Cardiac function as measured by echocardiography ($n = 6$ biological replicates, except DKO + δA ($n = 5$) and DKO + δ9 ($n = 3$)). Significance was tested using a one-way ANOVA with Tukey's multiple comparisons test. *P* values versus WT: *Rbm20* KO + PBS = <0.0001, DKO + Luc = 0.8970, DKO + δA = 0.0015, DKO + δB = 0.0004, DKO + δC = 0.0002, DKO + δ4 = <0.0001 and DKO + δ9 = 0.0448. **e**, H&E and picrosirius red staining. Scale bars, 1 mm (two-chamber view), 100 µm (picrosirius red). Data in graphs are presented as mean values ± s.e.m.

two doses of hesperadin compared to WT hearts (Fig. 5a). DEGs in the heterozygous *Rbm20*-p.Arg636Gln KI mouse hearts included increased expression of cardiac stress markers such as *Anf*, and decreased expression of *Myh7b* (Fig. 5b). The latter is in line with a previous observation by Ihara et al.[26], who similarly found a loss of *Myh7b* in a *Rbm20* KI mouse model. We then overlapped DEGs in DMSO-treated mice with DEGs in hesperadin-treated mice, and found that only ~55% of these DEGs were shared between groups, indicating that the transcriptional response differs between the DMSO-treated and hesperadin-treated mice (Fig. 5c). Gene Ontology enrichment of DEGs uniquely upregulated in heterozygous *Rbm20*-p.Arg636Gln KI mouse hearts revealed an increase in calmodulin-dependent protein kinase activity in the heterozygous *Rbm20*-p.Arg636Gln KI, and this enrichment was absent in the hesperadin-treated heterozygous *Rbm20*-p.Arg636Gln KI mouse hearts (Fig. 5d and Extended Data Fig. 10). Next, we performed phosphoproteomics, and found 782 phosphorylation events in 414 proteins that were increased in the hearts of heterozygous *Rbm20*-p.Arg636Gln KI mice (Fig. 5e). Kinase enrichment analysis showed that CAMK2D was one of the most enriched kinases predicted to be responsible for these phosphorylation events (Fig. 5f). Among those, we then identified the phosphorylation events that were decreased with treatment of hesperadin. We found 365 events in 251 proteins, demonstrating that the phosphorylation of approximately half of these events was reversed (cluster 1; Fig. 5e). Moreover, kinase enrichment analysis of cluster 1 identified CAMK2D as one of the enriched kinases predicted to be responsible for these phosphorylation events (Fig. 5g). Notably, AURKB, which is also inhibited by hesperadin, was likewise identified to be enriched in this cluster. Overall, these data show that CAMK2D activity was increased in *Rbm20*-p.Arg636Gln KI mice, and that hesperadin effectively inhibited this activity. Taken together, our results suggest that pharmacological inhibition of CAMK2D is a promising therapeutic approach for patients with *RBM20* mutations.

Discussion

In this study, we investigated the relative contribution of CAMK2D to the detrimental phenotypes in RBM20 cardiomyopathy, and we established that heart failure in RBM20 cardiomyopathy depends on CAMK2D. AAV9-mediated reexpression of single *Camk2d* splice variants in *Rbm20/Camk2d* DKO mice reintroduces cardiac dysfunction irrespective of which splice isoform is reexpressed, unmasking that specific CAMK2D overactivation rather than mis-splicing underlies the severe phenotype. This shows that RBM20 cardiomyopathy is not only caused by mis-splicing of RBM20 targets, including *TTN*, but to a large extent by CAMK2D activation. The fact that reexpression of all CAMK2D splice variants reintroduce cardiac dysfunction suggests there is considerable functional overlap between the different CAMK2D splice isoforms. Multiple observations support this hypothesis: (1) the shift in CAMK2D splice isoform in mouse and human after loss of functional RBM20 is different, even though the cardiac phenotype is similar; (2) reexpression of all cardiac splice isoforms is sufficient to reintroduce cardiac dysfunction in *Rbm20/Camk2d* DKO mice; and (3) almost all *CAMK2D* splice variants were found in the nuclear fraction in both WT and *Rbm20* KO mouse hearts, an observation that has been made before[17]. The underlying mechanism of how CAMK2D localizes primarily to the nucleus,

https://doi.org/10.1038/s44161-026-00818-2

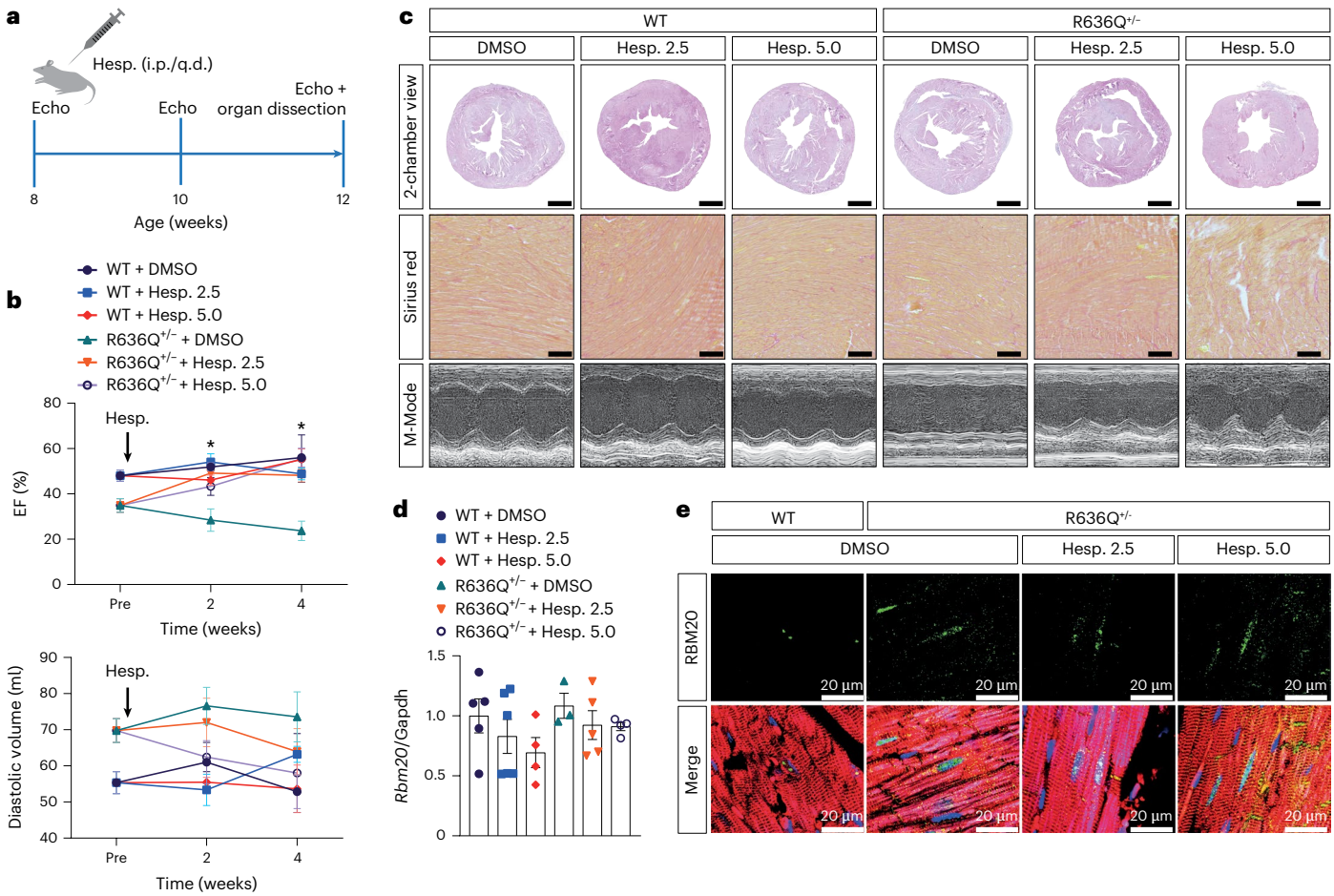

Fig. 4 | CAMK2D inhibition with hesperadin alleviates cardiac dysfunction in *Rbm20*-p.Arg636Gln KI mice. a, Experimental setup. i.p., intraperitoneal; q.d., quaque die (once daily). **b**, Cardiac function and diastolic volume as measured by echocardiography ($n = 6$ biological replicates, except WT + DMSO and p.Arg636Gln$^{+/-}$ + DMSO ($n = 7$) and p.Arg636Gln$^{+/-}$ + hesperadin (Hesp.) 5.0 ($n = 5$). Significance was tested per time point using a one-way ANOVA with Tukey's multiple comparisons test. *P* value of p.Arg636Gln$^{+/-}$ + DMSO at 2 weeks versus p.Arg636Gln$^{+/-}$ + Hesp. 5.0 = 0.0030 and versus p.Arg636Gln$^{+/-}$ + Hesp. 5.0 = 0.0779, at 4 weeks versus p.Arg636Gln$^{+/-}$ + Hesp. 2.5 = 0.0048 and versus p.Arg636Gln$^{+/-}$ + Hesp. 5.0 = 0.0004. **c**, H&E and picrosirius red staining. Scale bars, 1 mm (two-chamber view), 100 µm (picrosirius red). **d**, qPCR of *Rbm20* ($n = 5$ biological replicates for WT + DMSO and p.Arg636Gln$^{+/-}$ + Hesp. 2.5, $n = 7$ for WT + Hesp. 2.5, $n = 4$ for WT + Hesp. 5.0 and p.Arg636Gln$^{+/-}$ + Hesp. 5.0 and $n = 3$ for p.Arg636Gln$^{+/-}$ + DMSO). **e**, Immunohistochemistry of RBM20 in left ventricular tissue. Data in graphs are presented as mean values ± s.e.m.

independent of the inclusion of the nuclear localization signal NLS in exon 14, remains to be elucidated. Nevertheless, it will be important to further investigate the potential functional differences between the different splice isoforms of CAMK2D as AAV-mediated overexpression cannot precisely be controlled and variations in the amount and mosaic patterns may limit the interpretation of the approach that was used in this study. Importantly, we show that pharmacological inhibition of CAMK2D in *Rbm20*-p.Arg636Gln KI mice has striking therapeutic effects on structural remodeling and cardiac dysfunction. Treatment of patients with *RBM20* mutations currently relies on the 'fantastic four' (beta blockers, ACE inhibitors/AT1 antagonists, SGLT2 inhibitors and mineralocorticoid antagonists)[34]. As a specific approach, gene editing has been used in mouse models to correct disease-causing mutations in *RBM20* (refs. 27,35). However, technical and safety hurdles with respect to successful AAV-mediated gene transfer and potentially CRISPR–Cas9 toxicity need to be overcome to translate this concept into the clinic. Moreover, this approach needs to be personalized due to the vast number of different variants that have been identified in the *RBM20* gene, which would require a costly individualized approach, limiting the feasibility. Here, we propose that pharmacological CAMK2D inhibition is a novel tailored approach to treat patients affected by heart failure in *RBM20* cardiomyopathy with different pathogenic variants. The use of hesperadin to inhibit CAMK2D in patients may not be favorable because even though it inhibits CAMK2D more than other CAMK2 isozymes (20–200 fold more selective), it also inhibits other kinases such as Aurora kinase B, AMPK, Lck, MKK1, MAPKAP-K1, CHK1 and PHK[33,36]. The current study, however, serves as a proof-of-principle study that now calls for validation with a selective CAMK2 inhibitor. After 35 years of work on CAMK2 and the development of multiple CAMK2 inhibitors (see ref. 37 for a review), there has not been a CAMK2-selective inhibitor that made it to clinical practice. The only CAMK2 inhibitor that is currently used in clinical practice is ruxolitinib, but this is for its better-known role as a JAK inhibitor in patients with myelofibrosis[37–39]. Therefore, it comes with great promise that a specific and selective CAMK2 inhibitor is currently in a phase II clinical trial (ClinicalTrials.gov registration: NCT06005428)[40,41]. Here, we used both a *Rbm20* KO model, which has only loss of splicing, and a *Rbm20* KI model, which has the additional detrimental cytoplasmic granule formation. In both cases, CAMK2D inhibition, either genetic in the KO model or pharmacological in the KI model, improved cardiac function. This suggests that pharmacological CAMK2D inhibition in RBM20 cardiomyopathy holds promise independent of the type of mutation in the patient, whether this is a purely loss-of-function variant (for example, truncating variant) or a mislocalizing variant (for example, RSRSP variant). In addition,

https://doi.org/10.1038/s44161-026-00818-2

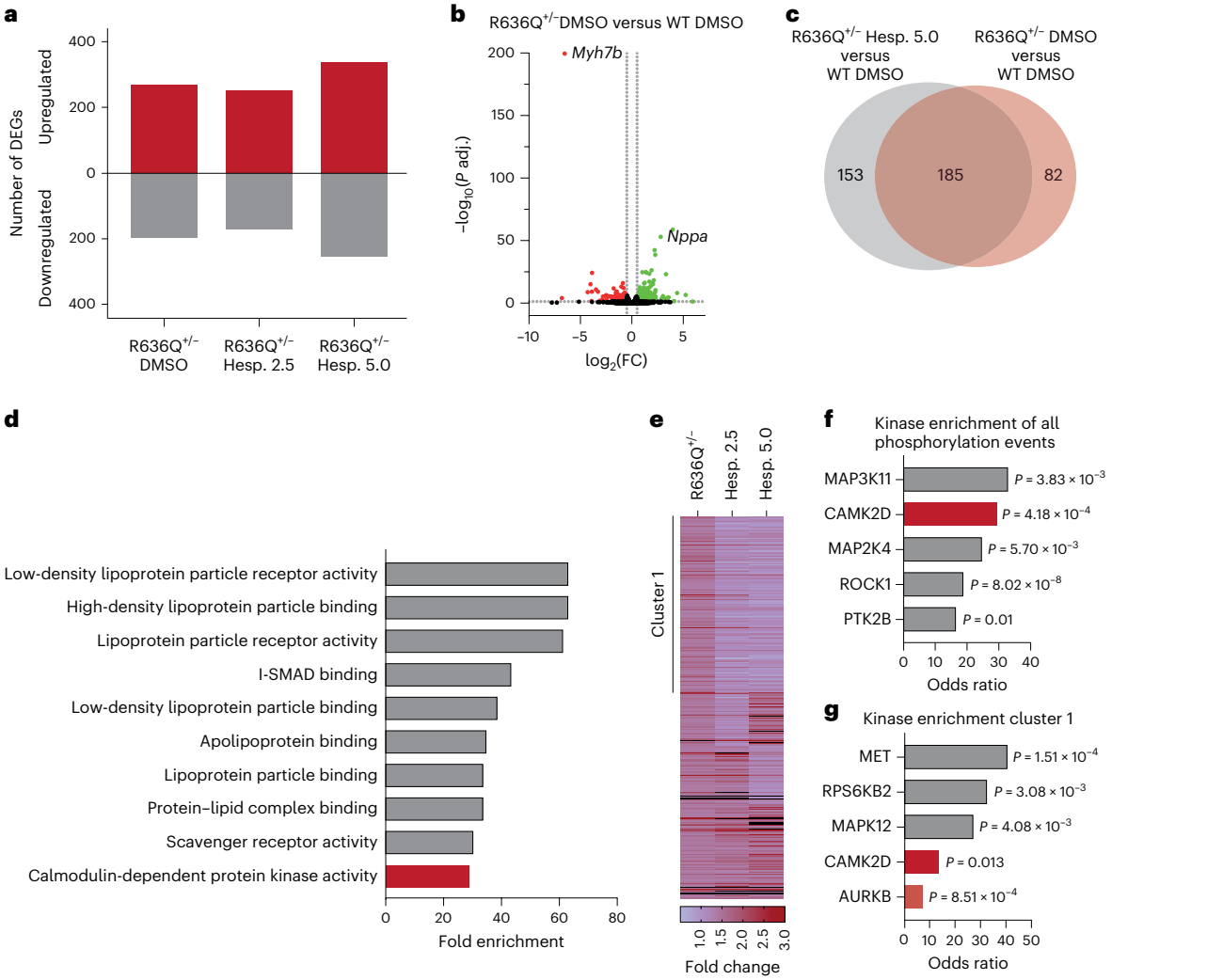

Fig. 5 | Hesperadin treatment inhibits CAMK2D activity in *Rbm20*-p.Arg636Gln KI mice. a, Number of DEGs in vehicle-treated and hesperadin-treated heterozygous *Rbm20*-p.Arg636Gln KI mice as compared to vehicle-treated WT mice. **b**, Volcano plot of DEGs (fold change (FC) > 0.5, adjusted *P* value (*P* adj. < 0.05)) in heterozygous *Rbm20*-p.Arg636Gln KI mouse hearts. **c**, Venn diagram of upregulated genes in vehicle-treated and hesperadin-treated (5 µg per kg body weight) heterozygous *Rbm20*-p.Arg636Gln KI mouse hearts. **d**, Gene Ontology enrichment analysis of genes uniquely upregulated in vehicle-treated heterozygous *Rbm20*-p.Arg636Gln KI mouse hearts. **e**, Heat map of phosphorylation events in vehicle-treated and hesperadin-treated heterozygous *Rbm20*-p.Arg636Gln KI mouse hearts. With fold change set to ≥1.3, we observed 782 events in 414 proteins. **f**, Kinase enrichment analysis of phosphorylation events increased (FC ≥ 1.3, false discovery rate (FDR) < 0.05) in heterozygous *Rbm20*-p.Arg636Gln KI mouse hearts. **g**, Kinase enrichment analysis of phosphorylation events (FC ≥ 1.3, FDR < 0.05) in cluster 1 (365 events in 251 proteins).

CAMK2 activation contributes to multiple forms of heart disease, for example, pressure-induced heart failure, post-infarction remodeling and atrial/ventricular arrhythmia[16]. It must be noted, however, that CAMK2 activation is not a universal hallmark of all cardiac diseases; for example, in a new mouse model with the human DCM-causing mutation *LMNA*-p.Lys117fs, we do not observe CAMK2 activation. Our data suggest that CAMK2D inhibition can now be tested as a cause-directed DCM therapy for RBM20 cardiomyopathy. To do so, large cardiomyopathy registries have been established where the included patients undergo whole-genome sequencing to identify the underlying disease mutations that could be selected as patients for a first tailored phase IIb/III trial[42]. Due to the here-described CAMK2-dependent etiology of RBM20 cardiomyopathy, it is expected that a clinical trial would be sufficiently powered by the inclusion of a lower number of patients than in past clinical trials that included patients with heart failure who have heterogeneous etiologies[43–46]. The development and success of mavacamten for oHCM, culminating in the pivotal EXPLORER_HCM trial, has demonstrated that efficacy can be shown in a relatively small cohort of only 251 randomized patients, of which 123 received mavacamten[7,47]. Following this strategy, pharmacological CAMK2 inhibition might become the first cause-directed therapy for RBM20 cardiomyopathy on top of the general standard heart failure medication.

Methods

Animal experiments

This study adheres to the EU Directive (2010/63/EU) and received approval from the Institutional Animal Care and Use Committee at the Regierungspräsidium Karlsruhe, Germany (approval numbers G120-17, G233/17 and G225/20). Hesperadin treatment in *Rbm20*-p.Arg636Gln KI mice conformed to the EMBL guidelines for the Use of Animals in Experiments and was reviewed and approved by the Institutional Animal Care and Use Committee. At the conclusion of the experiments, mice were euthanized via cervical dislocation. Global *Rbm20* KO mice (FVB genetic background), global *Camk2d* KO mice (C57BL/6N genetic background) and *Rbm20*-p.Arg636Gln mice (C57BL/6J genetic background) were previously generated[14–16]. *LMNA*-p.Lys117fs mice

(C57BL/6N genetic background) were generated by insertion of a +1 frameshift mutation causing a premature stop codon using CRISPR–Cas9. The single guide RNA 5′-agttcaaggagctgaaggct-3′ targeting the mouse genomic *LMNA* locus was designed using CRISPOR (http://crispor.tefor.net/)[48] and transcribed from GeneArt Strings DNA Fragments (Thermo Scientific) using the MEGAshortscript T7 Transcription Kit (Thermo Scientific). After in vitro transcription, the RNA was purified using the MEGAclear Transcription Clean-Up Kit (Thermo Scientific). The single guide RNA (25 ng µl^{-1}), a 120-bp single-stranded homology-directed repair template oligonucleotide (5′-aggagcgcgccgcctccagctagagctgagcaaagtgcgtgaggagttcaaggagctggaaggctcggtgagtgaggcccggccggccggcaccagggaggcagcagtcgcctgtaact-3′; 3 µM), 25 ng µl^{-1} GeneArtTM CRISPR Nuclease mRNA (Thermo Scientific) and 25 ng µl^{-1} EnGen Spy Cas9 nuclear localization signal (NEB) diluted in injection buffer (5 mM Tris, 0.1 mM EDTA, pH 7.4, sterile filtered) were injected into zygotes from superovulated female mice (Charles River Laboratories) and implanted into foster mice. Positive founder mice were backcrossed for at least six generations. *Rbm20*/*Camk2d* DKO mice were obtained by crossing *Rbm20* KO and *Camk2d* KO mice. Mice were given normal chow and water ad libitum, and kept on a 12-h light–dark cycle. Hesperadin (SelleckChem, S1529) was dissolved in 5% DMSO, 40% PEG300, 5% Tween 80 and 50% double-distilled water. Mice were intraperitoneally injected daily with vehicle (5% DMSO, 40% PEG300, 5% Tween 80 and 50% double-distilled water), 2.5 µg per kg body weight or 5 µg per kg body weight hesperadin.

Echocardiography and catecholamine challenge

Mice were anesthetized using 1–1.5% isoflurane (Baxter Deutschland). Anesthesia depth was confirmed by assessing reflexes before conducting echocardiography, and heart rate and respiratory rate were monitored continuously. To maintain body temperature, mice were placed on a heating pad. Imaging was performed using the Vevo 2100 or 3100 Imaging System with an MS400 Transducer (FUJIFILM VisualSonics). For ventricular function, B-mode and M-mode images of the short and long axis at the midpapillary muscle level were captured. Atrial echocardiograms were performed as previously described[49]. Echocardiographic parameters were calculated using the VisualSonics VevoLab software's LV trace tool with the Teicholz equation, based on at least five contraction cycles. Arrhythmia induction was done by intraperitoneal injection of 2 mg per kg body weight epinephrine and 120 mg per kg body weight caffeine in male mice, after which mice were monitored for survival.

Exercise tolerance test

Endurance exercise capacity was assessed at 10 weeks of age using graded maximal treadmill running. Mice were trained for 3 days on the treadmill (15 min per day at 16 cm s^{-1}) before the exercise tolerance test. For the exercise tolerance test, mice were placed on the treadmill at a 20° incline starting at 16 cm s^{-1}. After 5 min, the treadmill speed was increased by 3 cm s^{-1}, after which the speed was again increased by 3 cm s^{-1} every 2 min. The treadmill test was terminated when mice sustained contact with a shock grid for 5 s, which we defined as the point of exhaustion.

Pressure–volume loops

Mice were anesthetized with 5% isoflurane, intubated and then maintained at 1.5% isoflurane with ventilation. An apical approach was used to perform pressure–volume measurements using a Millar MPVS Ultra setup equipped with a mouse 1.4-F catheter (SPR 839, Millar Instruments) as described previously[50]. Load-independent parameters were obtained by inferior vena cava occlusion during a pause in ventilation. Data were analyzed using LabChart Pro 8.1.30 software.

Isometric force measurements in skinned cardiomyocytes

Frozen ventricular tissue samples from WT, *Rbm20* KO, *Camk2d* KO and DKO mice (n = 4 hearts per genotype) were thawed in relaxing solution. Cardiomyocytes were mechanically isolated by gentle tissue disruption as described previously[51]. Isolated cardiomyocytes were chemically permeabilized by incubation for 5 min in relaxing solution containing 0.5% (vol/vol) Triton X-100 and subsequently mounted between a force transducer and a servo motor (Aurora Scientific). Isometric force measurements were performed in single cardiomyocytes at two sarcomere lengths. The shorter length (~1.8 µm) was chosen to fall within the physiological operating range observed in vivo in mice (~1.90 µm in diastole to ~1.68 µm in systole, as determined by in vivo cardiac nano-imaging of beating mouse hearts[31]), whereas the longer length (~2.2 µm) provided supraphysiological stretch to assess length-dependent activation (that is, the Frank–Starling cellular basis). Average sarcomere length during each contraction was determined by spatial Fourier transformation of the striation pattern. Absolute force was normalized to cardiomyocyte cross-sectional area and expressed as tension (kN/m^2). Passive force (F_{pas}) was determined in relaxing solution by shortening the cardiomyocyte to 70% of its initial length (30% slack). Active tension (F_{max}) at each Ca^{2+} concentration was calculated as: $F_{max} = F_{total} - F_{pas}$. The composition of all solutions was calculated using a computer program described previously[51]. The pH of all solutions was adjusted to 7.1 at 15 °C with potassium hydroxide, and ionic strength was adjusted to 180 mM with KCl. The relaxing solution contained (final free concentrations): 2 mM free Mg^{2+}, 10 mM MgATP, 20 mM EGTA, 10 mM BES and 10 mM phosphocreatine. The maximal Ca^{2+}-activating solution consisted of 2 mM free Mg^{2+}, 10 mM MgATP, 20 mM EGTA, 10 mM BES and 32 µM free Ca^{2+}. Submaximal Ca^{2+}-activating solutions were obtained by mixing the maximal Ca^{2+}-activating and relaxing solutions at appropriate ratios, assuming an apparent stability constant of the Ca^{2+}–EGTA complex of 10. Tension–Ca^{2+} (Tension–pCa) relationships were fitted by nonlinear regression to a modified Hill equation using GraphPad Prism 7 (GraphPad Software) according to equation (1):

$$P\left(Ca^{2+}\right)/P_0 = \left[Ca^{2+}\right]^{nH} / \left(K^{nH} + \left[Ca^{2+}\right]^{nH}\right) \quad (1)$$

where P (Ca^{2+}) is steady-state active tension at a given free [Ca^{2+}]. P_0 is maximal active tension at saturating [Ca^{2+}], nH is the Hill coefficient (steepness), and K is the [Ca^{2+}] at which force is half-maximal (0.5 × P_0). Myofilament Ca^{2+} sensitivity is reported as pCa_{50}, defined as $-\log_{10}[K]$.

RNA isolation and qPCR + RT–PCR

Total RNA was extracted from left ventricular mouse heart tissue using TRIzol reagent (Thermo Fisher). cDNA was synthesized from 1 µg of RNA using the primaREVERSE RT-Kit (Steinbrenner Laborsysteme, SL-9540-1000), following the manufacturer's instructions. RT–PCR was conducted with HOT FIREPol DNA Polymerase (Solis BioDyne) according to the manufacturer's protocol, followed by gel electrophoresis on 1.5% agarose gels. RT–qPCR was carried out using PowerUp SYBR Green Master Mix (Thermo Fisher) on a Lightcycler 480 II system (Roche), with each sample run in technical duplicates. Data were analyzed using LinRegPCR version 2018.030, and primer sequences are available in Supplementary Table 2.

RNA-seq

Total RNA from left ventricular tissue of *Rbm20/Camk2d* KO mice was depleted from ribosomal RNA, polyA-enriched, fragmented and paired-end sequenced at BGI (Hong Kong). Total RNA from left ventricular tissue from hesperadin-treated mice was extracted and sequence libraries were prepared using SMART-Seq Total RNA pico input (Takara Bio) and sequenced in paired-end mode on AVITI (PE75, Element Biosciences). RNA-seq reads were aligned to mouse genome reference (mm10 GRCm38) using the Rsubread R package. Quality control of the reads was performed using Fastqcr and Rqc packages, while adaptor trimming was conducted with Trimmomatic using standard parameters. For data processing and analysis, we used an

R-based pipeline utilizing BiocManager for package management and ShortRead for sequence manipulation and reading. Differential gene expression analysis was performed using DESeq2 (ref. 52). Functional enrichment analysis of DEGs was conducted using the ClusterProfiler package to identify overrepresented biological pathways, molecular functions and cellular components in the Gene Ontology database and relevant pathways in the KEGG database[53]. Splice junction counts were extracted from read aligments using Regtools with default parameters and annotated with the respective transcript identifier, for expressed transcripts (mean transcripts per million > 1)[54].

Protein isolation and western blotting

Tissue was homogenized in RIPA buffer (50 mM Tris-HCl pH 8, 150 mM NaCl, 1% NP-40, 0.5% sodium deoxycholate, 0.1% SDS) supplemented with protease inhibitor cocktail (Roche) using a TissueLyser II (Qiagen). Protein concentration was measured using a BCA assay (Pierce). Western blotting was performed following standard protocols. Antibodies used were anti-CAMK2 (611293, BD Biosciences), anti-GAPDH (MAB374, Sigma) and anti-Flag (F1804, Sigma). Quantification of western blots was done using ImageJ software.

Phosphoproteomics

For phosphoproteomics on the *Rbm20/Camk2d* DKO mice, left ventricular tissue of 10-week-old mice was lysed in RIPA buffer supplemented with a protease inhibitor (S8820, MilliporeSigma) and a phosphatase inhibitor (P5726, MilliporeSigma). Proteins were digested using Lysyl Endopeptidase (Lys-C, FUJIFILM Wako Pure Chemicals) and trypsin (MilliporeSigma). Desalting was carried out using Sep-Pak C18 columns (Waters), preconditioned with 100% acetonitrile (ACN) and rinsed twice with 0.1% trifluoroacetic acid (TFA). Samples were eluted in 60% ACN–0.1% TFA, and then dried. Phosphopeptides were enriched using the High-Select TiO2 Phosphopeptide Enrichment Kit (A32993, Thermo Fisher). Proteomic analysis used an Easy nLC 1000 ultrahigh-performance liquid chromatography system coupled to a Q Exactive Plus mass spectrometer (Thermo Fisher). Peptides were dissolved in solvent A (0.1% formic acid), loaded with an autosampler and separated on custom-made 50-cm fused silica columns (75-µm internal diameter, packed with 2.7-µm C18 Poroshell beads (Agilent)) at a flow rate of 0.75 µl min^{-1}. Gradients of 90 min for phosphoproteomics and 240 min for whole proteome analysis were applied, with peptides eluted at 250 nl min^{-1}. The eluted peptides were ionized via nanoelectrospray and introduced into the mass spectrometer's heated transfer capillary. The instrument was operated in a data-dependent acquisition mode. Full mass spectrometry (MS) scans (300–1,750 *m/z*) were performed in the Orbitrap at a resolution of 70,000, with an automated gain control (AGC) target of 3×10^6 ions and a maximum injection time of 20 ms. A dynamic exclusion window of 20 s was used, and the top ten most intense peaks ($z \geq 2$) from each scan were fragmented in the high-energy collision-induced dissociation cell with a normalized collision energy of 25%. MS/MS scans were acquired at a resolution of 17,500. Data were processed using MaxQuant software and its integrated Andromeda search engine, with default settings and Phospho (STY) included as a variable modification. Statistical analyses were conducted using Perseus.

For phosphoproteomics on hesperadin-treated *Rbm20*-p.Arg636Gln$^{+/-}$ mice, sample preparation was performed as described[55]. Briefly, mouse heart left ventricular tissue was lysed in 500 µl of lysis buffer consisting of 100 mM Tris-HCl (pH 8.5), 7 M urea, 1% Triton X-100, 5 mM Tris(2-carboxyethyl)phosphine hydrochloride, 55 mM 2-chloroacetamide, 10 U ml^{-1} DNase I, 1 mM magnesium chloride, 1 mM sodium orthovanadate, Phosphatase Inhibitor Cocktail 2 (Sigma-Aldrich) and Halt Protease Inhibitor Cocktail (Thermo Fisher). Lysates were sonicated for 45 min (20 s on, 40 s off) at 4 °C, using a Bioruptor (Diagenode). Cell debris was removed, benzonase (final concentration 1%) was added to the cleared supernatant, and the mixture was incubated at room temperature for 30 min. For each sample, 500 µg of protein was precipitated. The pellet was subsequently resuspended in 50 mM HEPES/sodium hydroxide (pH 8.5), 1% sodium deoxycholate, 5 mM Tris(2-carboxyethyl)phosphine hydrochloride and 30 mM 2-chloroacetamide. Proteins were digested overnight at room temperature with trypsin added at a protein-to-enzyme ratio of 50:1. Digestion was stopped by the addition of TFA to a final concentration of 1%. Sodium deoxycholate was precipitated for 15 min at room temperature and the samples were centrifuged at 17,000*g* for 10 min. Peptides were desalted using Oasis HLB 96-well plates (30 µm, Waters) under gravity flow. Washing was performed with buffer A (MS-grade water, 0.1% formic acid) and peptides were eluted using buffer B (80% ACN, 0.1% formic acid). Phosphopeptide enrichment was performed as previously described[56]. Briefly, peptides were resuspended in IMAC loading solvent (80% ACN, 0.4% TFA). A small aliquot of each sample was used for full proteome analysis, while the remaining peptides were subjected to phosphopeptide enrichment using the KingFisher Apex platform (Thermo Fisher) and magnetic Fe-NTA beads (Cube Biotech). Enriched phosphopeptides were eluted with 0.2% dimethylamine in 80% ACN to facilitate subsequent TMT labeling. Peptides were modified with TMTpro labeling reagent (Thermo Fisher Scientific)[57]. In short, 0.5 mg reagent was dissolved in 45 µl ACN (100%) and 8 µl of stock was added and incubated for 1 h room temperature. Followed by quenching the reaction with 5% hydroxylamine for 15 min room temperature. Samples were combined for multiplexing and an OASIS HLB µElution Plate (Waters) was used for further sample cleanup. Offline high pH reverse-phase fractionation was performed using an Agilent 1200 Infinity high-performance liquid chromatography system equipped with a quaternary pump, degasser, variable wavelength UV detector (set to 254 nm), Peltier-cooled autosampler and fraction collector (both set at 10 °C for all samples). The column was a Gemini C18 column (3 µm, 110 Å, 100 × 1.0 mm, Phenomenex) with a Gemini C18, 4 × 2.0 mm SecurityGuard (Phenomenex) cartridge as a guard column. The solvent system consisted of 20 mM ammonium formate (pH 10.0) (A) and 100% ACN as mobile phase (B). The separation was accomplished at a mobile phase flow rate of 0.1 ml min^{-1} using the following linear gradient: 100% A for 2 min, from 100% A to 35% B in 59 min, to 85% B in a further 1 min, and held at 85% B for an additional 15 min, before returning to 100% A and re-equilibration for 13 min. Forty-eight fractions were collected along with the liquid chromatography separation that were subsequently pooled into 12. Pooled fractions were dried under vacuum centrifugation. An UltiMate 3000 RSLC nano LC system (Dionex) fitted with a trapping cartridge (µ-Precolumn C18 PepMap 100, 5 µm, 300 µm internal diameter × 5 mm, 100 Å, Thermo Fisher Scientific) and an analytical column (nanoEase M/Z HSS T3 column 75 µm × 250 mm C18, 1.8 µm, 100 Å, Waters). Trapping was carried out with a constant flow of trapping solution (0.05% TFA in water) at 30 µl min^{-1} onto the trapping column for 6 min. Subsequently, peptides were eluted via the analytical column running solvent A (3% DMSO, 0.1% formic acid in water) with a constant flow of 0.3 µl min^{-1}, with an increasing percentage of solvent B (3% DMSO, 0.1% formic acid in ACN). Each fraction of the full proteome was measured for 120 min and each fraction of the phopshoproteme for 90 min. The peptides were introduced into a Orbitrap Fusion Lumos Tribrid Mass Spectrometer via a Pico-Tip Emitter 360 µm outer diameter × 20 µm internal diameter; 10 µm tip (CoAnn Technologies) and an applied spray voltage of 2.2 kV. The capillary temperature was set at 275 °C. A full mass scan was acquired with a mass range of 375–1,500 *m/z* (to 1,650 *m/z* for phosphopeptides) in profile mode in the Orbitrap with a resolution of 120,000. The filling time was set at a maximum of 50 ms with an AGC target set to standard, which allows an absolute AGC target of 4×10^5 ions. Data-dependent acquisition was performed with the resolution of the Orbitrap set to 30,000, with a fill time of 94 ms (110 ms for phoshopeptides) and a limitation of 1×10^5 ions. A normalized collision energy of 34 was applied. MS2 data were acquired in profile mode. The isolation window of the

quadrupole was set to 0.7 *m/z*. A dynamic exclusion time of 60 s (20 s for the phosphopeptides) was used. Fragpipe v22.1 with MSFragger v4.1 was used to process the acquired data, which was searched against the *Mus musculus* Uniprot proteome database (UP000000589, ID10090, 21986 entries, released October 2022) with common contaminants and reversed sequences included[58]. The following modifications were considered as fixed modification: Carbamidomethyl (C) and TMT6 or 10 (K). The following modifications were considered as variable modifications: acetyl (protein N-term), oxidation (M) and TMT6 or 10 (N-term), for the phosphoproteome specifically phosphorylation on STY. For the MS1 and MS2 scans, a mass error tolerance of 20 ppm was set. Further parameters were: Trypsin as protease with an allowance of maximum two missed cleavages; minimum peptide length of seven amino acids; at least two unique peptides were required for a protein identification. The FDR on the peptide and protein level was set to 0.01. Data were then analyzed as follows: the raw output files of FragPipe (psm.tsv for phospho data and protein.tsv files for input data) were processed using the R programming language (ISBN 3-900051-07-0). Only peptide spectral matches (PSMs) with a phosphorylation probability greater than 0.5 and proteins with at least two unique peptides were considered for the analysis. Raw TMT reporter ion intensities were summed for all PSMs with the same phosphopeptide ID. For the input data, the reporter ion intensities were used as given in the protein.tsv output files. Phospho signals were also normalized by input abundance. For this the reporter ion intensity for each unique phosphor ID, condition and replicate was normalized according to equation (2):

$$\begin{aligned}&\mathrm{Norm.Intensity}_{\mathrm{phospho,gene,condition}}\\&=\frac{\frac{\mathrm{Intensity}_{\mathrm{phospho,gene,condition}}}{\mathrm{Intensity}_{\mathrm{input,gene,condition}}}}{\frac{\mathrm{median}(\mathrm{Intensity}_{\mathrm{phospho,gene}})}{\mathrm{median}(\mathrm{Intensity}_{\mathrm{input,gene}})}}\mathrm{median}(\mathrm{Intensity}_{\mathrm{phospho,gene}})\end{aligned}\quad(2)$$

Transformed summed TMT reporter ion intensities were first cleaned for batch effects using the 'removeBatchEffects' function of the limma package and further normalized using the vsn package (variance stabilization normalization)[59,60]. Missing values were imputed with the 'knn' method using the Msnbase package[61]. Proteins were tested for differential expression using the limma package. The replicate information was added as a factor in the design matrix given as an argument to the 'lmFit' function of limma. Also, imputed values were given a weight of 0.05 in the 'lmFit' function. A phosphopeptide or protein was annotated as a hit with an FDR smaller than 5% and a fold change of at least 100% and as a candidate with an FDR below 20% and a fold change of at least 50%. Gene Ontology enrichment analysis was performed using the 'compareCluster' function of the 'clusterProfiler' package[62]. The analysis was performed using 'org.Mm.eg.db' as the reference database. Kinase enrichment analysis was done using KEA3 (ref. 63).

Histochemistry

After overnight fixation in 4% paraformaldehyde, mouse hearts were embedded in paraffin using the HistoCore PEARL Tissue Processor and Arcadia Embedding Center (both from Leica Biosystems). Sections of 5 µm in thickness were cut, mounted on slides and dried on a hot plate for 30 min, followed by overnight drying in a 37 °C incubator. The sections were dewaxed twice in ROTIHistol (Carl Roth) for 10 min each, then rehydrated through a descending alcohol series (100% for 2 min, 96% for 2 min and 70% for 2 min) before being placed in distilled water. For H&E staining, a H&E fast staining kit (Carl Roth) was used according to the manufacturer's instructions. Sirius red staining was performed by immersing slides in picrosirius red solution (ScyTek Laboratories) for 30 min, followed by differentiation in acidified water (1% acetic acid) twice. The slides were then dehydrated using an ascending alcohol series (70% for 2 min, 96% for 2 min and 100% for 2 min), cleared in ROTIHistol, and mounted with 35 µl EUKITT neo mounting medium (ORSAtec). The slides were scanned using an Axioscan slide scanner (ZEISS).

Immunohistochemistry

Left ventricular sections were deparaffinized, rehydrated in a series of ethanol and boiled for 5 min in antigen unmasking solution (10 mM citrate, pH 6) in a pressure cooker. Sections were subsequently incubated with 4% normal goat serum in PBS with 0.1% Triton X-100 for 60 min at room temperature, and incubated with primary antibody in 4% normal goat serum in PBS overnight at 4 °C. Primary antibodies used were anti-RBM20 (PA5-58068, Thermo Fisher) and anti-alpha actinin (A7811, Sigma). Alexa Fluor 488- and Alexa Fluor 594-conjugated antibodies (Invitrogen) were used as secondary antibodies, and nuclei were visualized using DAPI (Sigma). Images were taken on a confocal microscope (Leica MICA, Leica Microsystems).

AAV generation and injection

The *Camk2d* splice variants were amplified from cDNA of mouse cardiac tissue, N-terminally FLAG-tagged and cloned into a p-GEM-T vector (Promega) and subsequently shuttled into the AAV genome plasmid pSSV9-TnT (kindly provided by O. Müller[64]) containing the cardiac-specific human troponin-T promotor, a chimeric human β-globin/immunoglobulin heavy chain intron and a SV40 polyadenylation signal. These constructs and a control humanized Renilla luciferase encoding plasmid, pSSV9-TnT-hrLuc, together with the adeno-helper plasmid, pdp9rs (kindly provided by J. Kleinschmidt), were used to generate single-stranded, pseudotyped ssAAV2/AAV9 in the AAVpro 293T cell line (Takara) as described previously[65]. In brief, each AAV genome plasmid was co-transfected with the adeno-helper plasmid using polyethylenimine. Seventy-two hours after transfection the supernatants and cells were harvested. The first underwent ammonium sulfate precipitation, while the latter were lysed by freeze–thaw cycles followed by DNase digestion. AAV vectors were then purified by ultracentrifugation on iodixanol step gradients, buffer exchanged to PBS, pooled and concentrated. The final vector stocks were quantified by qPCR using a plasmid standard curve. Mice were briefly anesthetized and injected retro-orbitally with 5×10^{12} viral genomes.

Reporting summary

Further information on research design is available in the Nature Portfolio Reporting Summary linked to this article.

Data availability

All RNA-seq data have been deposited in the Gene Expression Omnibus under accession number GSE311410.

References

1. Martin, S. S. et al. 2024 heart disease and stroke statistics: a report of US and global data from the American Heart Association. *Circulation* **149**, e347–e913 (2024).
2. Pinto, Y. M. et al. Proposal for a revised definition of dilated cardiomyopathy, hypokinetic non-dilated cardiomyopathy, and its implications for clinical practice: a position statement of the ESC working group on myocardial and pericardial diseases. *Eur. Heart J.* **37**, 1850–1858 (2016).
3. Haas, J. et al. Atlas of the clinical genetics of human dilated cardiomyopathy. *Eur. Heart J.* **36**, 1123–1135 (2015).
4. Hershberger, R. E., Hedges, D. J. & Morales, A. Dilated cardiomyopathy: the complexity of a diverse genetic architecture. *Nat. Rev. Cardiol.* **10**, 531–547 (2013).
5. Elliott, P. et al. Classification of the cardiomyopathies: a position statement from the European Society Of Cardiology Working Group on Myocardial and Pericardial Diseases. *Eur. Heart J.* **29**, 270–276 (2008).

6. Malone, E. R., Oliva, M., Sabatini, P. J. B., Stockley, T. L. & Siu, L. L. Molecular profiling for precision cancer therapies. *Genome Med.* **12**, 8 (2020).
7. Olivotto, I. et al. Mavacamten for treatment of symptomatic obstructive hypertrophic cardiomyopathy (EXPLORER-HCM): a randomised, double-blind, placebo-controlled, phase 3 trial. *Lancet* **396**, 759–769 (2020).
8. Lennermann, D., Backs, J. & van den Hoogenhof, M. M. G. New insights in RBM20 cardiomyopathy. *Curr. Heart Fail. Rep.* **17**, 234–246 (2020).
9. Maatz, H. et al. RNA-binding protein RBM20 represses splicing to orchestrate cardiac pre-mRNA processing. *J. Clin. Invest.* **124**, 3419–3430 (2014).
10. Guo, W. et al. RBM20, a gene for hereditary cardiomyopathy, regulates titin splicing. *Nat. Med.* **18**, 766–773 (2012).
11. Li, S., Guo, W., Dewey, C. N. & Greaser, M. L. Rbm20 regulates titin alternative splicing as a splicing repressor. *Nucleic Acids Res.* **41**, 2659–2672 (2013).
12. Radke, M. H. et al. Therapeutic inhibition of RBM20 improves diastolic function in a murine heart failure model and human engineered heart tissue. *Sci. Transl. Med.* **13**, eabe8952 (2021).
13. Methawasin, M. et al. Experimentally increasing the compliance of titin through RNA binding motif-20 (RBM20) inhibition improves diastolic function in a mouse model of heart failure with preserved ejection fraction. *Circulation* **134**, 1085–1099 (2016).
14. Zhang, M. et al. CaMKII-delta9 promotes cardiomyopathy through disrupting UBE2T-dependent DNA repair. *Nat. Cell Biol.* **21**, 1152–1163 (2019).
15. Duran, J., Nickel, L., Estrada, M., Backs, J. & van den Hoogenhof, M. M. G. CaMKIIδ splice variants in the healthy and diseased heart. *Front. Cell Dev. Biol.* **9**, 644630 (2021).
16. Hegyi, B., Bers, D. M. & Bossuyt, J. CaMKII signaling in heart diseases: emerging role in diabetic cardiomyopathy. *J. Mol. Cell Cardiol.* **127**, 246–259 (2019).
17. Mishra, S., Gray, C. B., Miyamoto, S., Bers, D. M. & Brown, J. H. Location matters: clarifying the concept of nuclear and cytosolic CaMKII subtypes. *Circ. Res.* **109**, 1354–1362 (2011).
18. Little, G. H., Bai, Y., Williams, T. & Poizat, C. Nuclear calcium/calmodulin-dependent protein kinase IIdelta preferentially transmits signals to histone deacetylase 4 in cardiac cells. *J. Biol. Chem.* **282**, 7219–7231 (2007).
19. Backs, J., Song, K., Bezprozvannaya, S., Chang, S. & Olson, E. N. CaM kinase II selectively signals to histone deacetylase 4 during cardiomyocyte hypertrophy. *J. Clin. Invest.* **116**, 1853–1864 (2006).
20. Odagiri, K. et al. Local control of mitochondrial membrane potential, permeability transition pore and reactive oxygen species by calcium and calmodulin in rat ventricular myocytes. *J. Mol. Cell Cardiol.* **46**, 989–997 (2009).
21. Maier, L. S. et al. Transgenic CaMKIIδC overexpression uniquely alters cardiac myocyte Ca^{2+} handling: reduced SR Ca^{2+} load and activated SR Ca^{2+} release. *Circ. Res.* **92**, 904–911 (2003).
22. Fenix, A. M. et al. Gain-of-function cardiomyopathic mutations in RBM20 rewire splicing regulation and re-distribute ribonucleoprotein granules within processing bodies. *Nat. Commun.* **12**, 6324 (2021).
23. Schneider, J. W. et al. Dysregulated ribonucleoprotein granules promote cardiomyopathy in RBM20 gene-edited pigs. *Nat. Med.* **26**, 1788–1800 (2020).
24. Kornienko, J. et al. Mislocalization of pathogenic *RBM20* variants in dilated cardiomyopathy is caused by loss-of-interaction with Transportin-3. *Nat. Commun.* **14**, 4312 (2023).
25. Wang, C. et al. *RBM20*^{S639G} mutation is a high genetic risk factor for premature death through RNA-protein condensates. *J. Mol. Cell Cardiol.* **165**, 115–129 (2022).
26. Ihara, K. et al. A missense mutation in the RSRSP stretch of *Rbm20* causes dilated cardiomyopathy and atrial fibrillation in mice. *Sci. Rep.* **10**, 17894 (2020).
27. Grosch, M. et al. Striated muscle-specific base editing enables correction of mutations causing dilated cardiomyopathy. *Nat. Commun.* **14**, 3714 (2023).
28. Lennermann, D. C. et al. Deep phenotyping of two preclinical mouse models and a cohort of RBM20 mutation carriers reveals no sex-dependent disease severity in RBM20 cardiomyopathy. *Am. J. Physiol. Heart Circ. Physiol.* **323**, H1296–H1310 (2022).
29. Zhu, C. et al. Single-molecule, full-length transcript isoform sequencing reveals disease-associated RNA isoforms in cardiomyocytes. *Nat. Commun.* **12**, 4203 (2021).
30. van den Hoogenhof, M. M. G. et al. RBM20 mutations induce an arrhythmogenic dilated cardiomyopathy related to disturbed calcium handling. *Circulation* **138**, 1330–1342 (2018).
31. Kobirumaki-Shimozawa, F. et al. Nano-imaging of the beating mouse heart in vivo: Importance of sarcomere dynamics, as opposed to sarcomere length per se, in the regulation of cardiac function. *J. Gen. Physiol.* **147**, 53–62 (2016).
32. Backs, J. et al. The delta isoform of CaM kinase II is required for pathological cardiac hypertrophy and remodeling after pressure overload. *Proc. Natl Acad. Sci. USA* **106**, 2342–2347 (2009).
33. Zhang, J. et al. Novel CaMKII-delta inhibitor hesperadin exerts dual functions to ameliorate cardiac ischemia/reperfusion injury and inhibit tumor growth. *Circulation* **145**, 1154–1168 (2022).
34. Heidenreich, P. A. et al. 2022 AHA/ACC/HFSA guideline for the management of heart Failure: executive summary: a report of the American College of Cardiology/American Heart Association Joint Committee on Clinical Practice Guidelines. *J. Am. Coll. Cardiol.* **79**, 1757–1780 (2022).
35. Nishiyama, T. et al. Precise genomic editing of pathogenic mutations in *RBM20* rescues dilated cardiomyopathy. *Sci. Transl. Med.* **14**, eade1633 (2022).
36. Hauf, S. et al. The small molecule hesperadin reveals a role for Aurora B in correcting kinetochore-microtubule attachment and in maintaining the spindle assembly checkpoint. *J. Cell. Biol.* **161**, 281–294 (2003).
37. Brown, C. N. & Bayer, K. U. Studying CaMKII: tools and standards. *Cell Rep.* **43**, 113982 (2024).
38. Reyes Gaido, O. E. et al. An improved reporter identifies ruxolitinib as a potent and cardioprotective CaMKII inhibitor. *Sci. Transl. Med.* **15**, eabq7839 (2023).
39. Plosker, G. L. Ruxolitinib: a review of its use in patients with myelofibrosis. *Drugs* **75**, 297–308 (2015).
40. Takagahara, S. et al. Abstract 12726: novel, potent, and highly selective calcium/calmodulin-dependent protein kinase II (CaMKII) inhibitors reduce substrate phosphorylation in rat hearts and prolong survival in a mouse model of severe heart failure. *Circulation* **148**, abstr. A12726 (2023).
41. A phase 2A, investigator & subject blinded, sponsor unblinded, placebo-controlled, clinical study to evaluate safety, tolerability, pharmacokinetics, pharmacodynamics of CRD-4730 in participants with catecholaminergic polymorphic ventricular tachycardia. *ClinicalTrials.gov* https://clinicaltrials.gov/study/NCT06005428?term=CRD-4730&viewType=Card&rank=2 (2023).
42. Seyler, C. et al. TranslatiOnal Registry for CardiomyopatHies (TORCH) - rationale and first results. *ESC Heart Fail.* **4**, 209–215 (2017).
43. Packer, M. et al. Cardiovascular and renal outcomes with empagliflozin in heart failure. *N. Engl. J. Med.* **383**, 1413–1424 (2020).
44. McMurray, J. J. et al. Angiotensin-neprilysin inhibition versus enalapril in heart failure. *N. Engl. J. Med.* **371**, 993–1004 (2014).

45. Effect of metoprolol CR/XL in chronic heart failure: metoprolol CR/XL randomised intervention trial in congestive heart failure (MERIT-HF). *Lancet* **353**, 2001–2007 (1999).
46. Pitt, B. et al. The effect of spironolactone on morbidity and mortality in patients with severe heart failure. Randomized Aldactone Evaluation Study Investigators. *N. Engl. J. Med.* **341**, 709–717 (1999).
47. Green, E. M. et al. A small-molecule inhibitor of sarcomere contractility suppresses hypertrophic cardiomyopathy in mice. *Science* **351**, 617–621 (2016).
48. Haeussler, M. et al. Evaluation of off-target and on-target scoring algorithms and integration into the guide RNA selection tool CRISPOR. *Genome Biol.* **17**, 148 (2016).
49. Zhang, M. J. et al. Atrial myopathy quantified by speckle-tracking echocardiography in mice. *Circ. Cardiovasc. Imaging* **16**, e015735 (2023).
50. Pacher, P., Nagayama, T., Mukhopadhyay, P., Batkai, S. & Kass, D. A. Measurement of cardiac function using pressure-volume conductance catheter technique in mice and rats. *Nat. Protoc.* **3**, 1422–1434 (2008).
51. Sequeira, V. et al. Synergistic role of ADP and Ca^{2+} in diastolic myocardial stiffness. *J. Physiol.* **593**, 3899–3916 (2015).
52. Love, M. I., Huber, W. & Anders, S. Moderated estimation of fold change and dispersion for RNA-seq data with DESeq2. *Genome Biol.* **15**, 550 (2014).
53. Xu, S. et al. Using clusterProfiler to characterize multiomics data. *Nat. Protoc.* **19**, 3292–3320 (2024).
54. Cotto, K. C. et al. Integrated analysis of genomic and transcriptomic data for the discovery of splice-associated variants in cancer. *Nat. Commun.* **14**, 1589 (2023).
55. Potel, C. M., Lin, M. H., Heck, A. J. R. & Lemeer, S. Defeating major contaminants in Fe^{3+}- immobilized metal ion affinity chromatography (IMAC) phosphopeptide enrichment. *Mol. Cell. Proteomics* **17**, 1028–1034 (2018).
56. Chang, A., Leutert, M., Rodriguez-Mias, R. A. & Villen, J. Automated enrichment of phosphotyrosine peptides for high-throughput proteomics. *J. Proteome Res.* **22**, 1868–1880 (2023).
57. Thompson, A. et al. TMTpro: design, synthesis, and initial evaluation of a proline-based isobaric 16-plex tandem mass tag reagent set. *Anal. Chem.* **91**, 15941–15950 (2019).
58. Kong, A. T., Leprevost, F. V., Avtonomov, D. M., Mellacheruvu, D. & Nesvizhskii, A. I. MSFragger: ultrafast and comprehensive peptide identification in mass spectrometry-based proteomics. *Nat. Methods* **14**, 513–520 (2017).
59. Ritchie, M. E. et al. limma powers differential expression analyses for RNA-sequencing and microarray studies. *Nucleic Acids Res.* **43**, e47 (2015).
60. Huber, W., von Heydebreck, A., Sultmann, H., Poustka, A. & Vingron, M. Variance stabilization applied to microarray data calibration and to the quantification of differential expression. *Bioinformatics* **18**, S96–S104 (2002).
61. Gatto, L. & Lilley, K. S. MSnbase-an R/Bioconductor package for isobaric tagged mass spectrometry data visualization, processing and quantitation. *Bioinformatics* **28**, 288–289 (2012).
62. Yu, G., Wang, L. G., Han, Y. & He, Q. Y. clusterProfiler: an R package for comparing biological themes among gene clusters. *OMICS* **16**, 284–287 (2012).
63. Kuleshov, M. V. et al. KEA3: improved kinase enrichment analysis via data integration. *Nucleic Acids Res.* **49**, W304–W316 (2021).
64. Werfel, S. et al. Rapid and highly efficient inducible cardiac gene knockout in adult mice using AAV-mediated expression of Cre recombinase. *Cardiovasc Res.* **104**, 15–23 (2014).
65. Jungmann, A., Leuchs, B., Rommelaere, J., Katus, H. A. & Muller, O. J. Protocol for efficient generation and characterization of adeno-associated viral vectors. *Hum. Gene Ther. Methods* **28**, 235–246 (2017).

Acknowledgements

We gratefully acknowledge M. Hagenmüller (Heidelberg University) for graphical assistance, E. Creemers (University of Amsterdam) for supplying the *Rbm20* KO mouse line, M. Oestringer (Heidelberg University) for coordination of the mouse lines, J. Pötzsch (Heidelberg University) for assistance with PV-loop experiments and J. Schwarz and F. Stein from the Proteomics Core at the EMBL Heidelberg for help with phosphoproteomics. We gratefully acknowledge the data storage service SDS@hd supported by the Ministry of Science, Research and the Arts Baden-Württemberg (MWK) and the the Deutsche Forschungsgemeinschaft (DFG, German Research Foundation) through grant INST 35/1503-1 FUGG. This publication was supported through state funds approved by the State of Baden-Wuerttemberg for the Innovation Campus Health and Life Science Alliance Heidelberg Mannheim, through the Helmholtz Institute for Translational AngioCardioScience (HI-TAC) and through grants from the DFG with grant number HO 6446/1 to M.M.G.v.d.H., and SFB1550 – Project ID 464424253: Collaborative Research Center 1550 (CRC1550) 'Molecular Circuits of Heart Disease' to M.M.G.v.d.H., J.B., L.M.S. and M.D. J.B. was supported by grants from the DZHK (Deutsches Zentrum für Herz-Kreislauf-Forschung - German Centre for Cardiovascular Research) and the BMBF (German Ministry of Education and Research). C.M. was supported by the DFG (SFB-1525, project no. 453989101, and grant Ma 2528/8-1). V.S. was supported by research funding from Bristol Myers Squibb and the DFG (project nos. 530849567 and 554784412). The funders had no role in the study design, data collection and analysis, decision to publish or preparation of the manuscript.

Author contributions

Conceptualization: M.M.G.v.d.H. and J.B. Methodology: M.M.G.v.d.H., J.D., T.B.-B., V.S., E.K., L.K., F.S., D.C.L., J.H., L.S., J.K., T.B. and M.D. Contributed materials: M.K., C.M., L.M.S. and C.D. Funding acquisition: M.M.G.v.d.H. and J.B. Supervision: M.M.G.v.d.H. and J.B. Writing—original draft: M.M.G.v.d.H., M.D. and J.B. Writing—review and editing: all authors.

Competing interests

V.S. received research funding from Bristol Myers Squibb unrelated to this work. C.M. is an advisory board member for Bristol Myers Squibb, Cytokinetics, Boehringer Ingelheim, AstraZeneca, Servier, Amgen, Novo Nordisk, Bayer, Novartis, Edwards and Berlin Chemie. The other authors declare no competing interests.

Additional information

Extended data is available for this paper at https://doi.org/10.1038/s44161-026-00818-2.

Supplementary information The online version contains supplementary material available at https://doi.org/10.1038/s44161-026-00818-2.

Correspondence and requests for materials should be addressed to Maarten M. G. van den Hoogenhof or Johannes Backs.

Peer review information *Nature Cardiovascular Research* thanks the anonymous reviewer(s) for their contribution to the peer review of this work. Peer reviewer reports are available.

[1]Heidelberg University, Medical Faculty Heidelberg, Institute of Experimental Cardiology, Heidelberg, Germany. [2]Heidelberg University Hospital, Department of Internal Medicine VIII, Heidelberg, Germany. [3]German Center for Cardiovascular Research (DZHK), Partner Site Heidelberg/Mannheim, Heidelberg, Germany. [4]Helmholtz-Institute for Translational AngioCardioScience (HI-TAC) of the Max Delbrück Center for Molecular Medicine in the Helmholtz Association (MDC) at Heidelberg University, Heidelberg, Germany. [5]Molecular Medicine Partnership Unit, European Molecular Biology Laboratory (EMBL) and Heidelberg University, Heidelberg, Germany. [6]Heidelberg University Hospital, Department of Internal Medicine III, Heidelberg, Germany. [7]Comprehensive Heart Failure Center, Department of Translational Science, University Clinic Würzburg, Würzburg, Germany. [8]Genome Biology Unit, European Molecular Biology Laboratory, Heidelberg, Germany. [9]Institute of Genetics and Cologne Excellence Cluster on Cellular Stress Responses in Aging-Associated Diseases (CECAD), University of Cologne, Cologne, Germany. [10]Department of Genetics, Stanford University School of Medicine, Stanford, CA, USA. ✉e-mail: maarten.hoogenhof@cardioscience.uni-heidelberg.de; johannes.backs@cardioscience.uni-heidelberg.de

https://doi.org/10.1038/s44161-026-00818-2

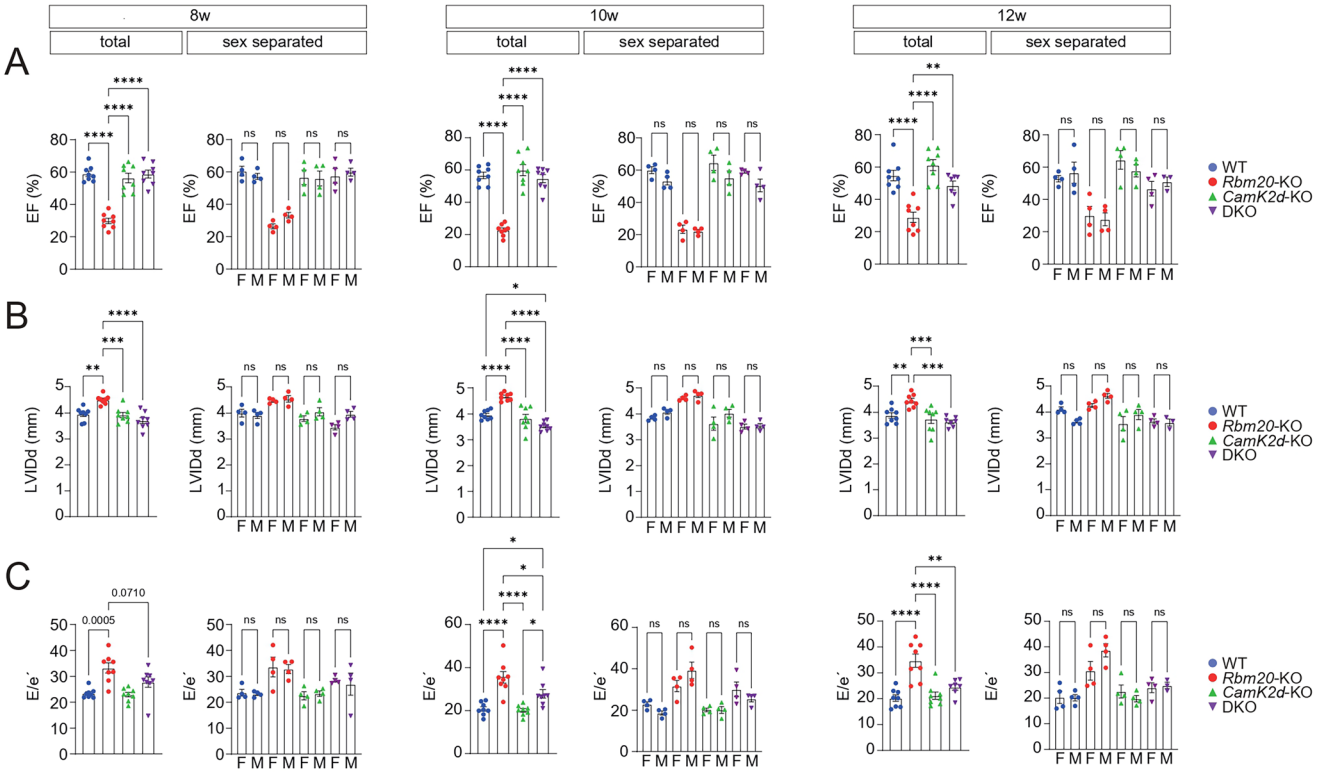

Extended Data Fig. 1 | Echocardiography of *Rbm20/Camk2d* DKO mice. **a**. Ejection fraction (EF) as measured by echocardiography at 8, 10, 12 weeks of age. **b**. Left ventricular internal diameter at diastole (LVIDd) as measured by echocardiography at 8, 10, 12 weeks of age. **c**. E/e' ratio as measured by echocardiography at 8, 10, 12 weeks of age. Left graphs (total) are all mice together (n = 8 biological replicates), right graphs are sex separated (n = 4 biological replicates). Significance was tested with a one-way ANOVA with Tukey's multiple comparisons test. P-values are * < 0.05, ** < 0.01, *** < 0.001, **** < 0.0001.

https://doi.org/10.1038/s44161-026-00818-2

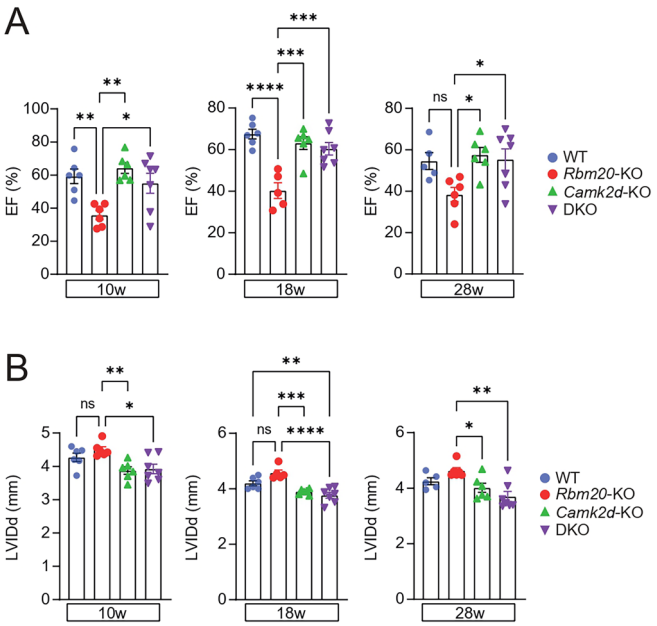

Extended Data Fig. 2 | Long-term echocardiography of *Rbm20/Camk2d* DKO mice. a. Ejection fraction (EF) as measured by echocardiography at 10, 18, and 28 weeks of age. **b**. Left ventricular internal diameter at diastole (LVIDd) as measured by echocardiography at 10, 18, and 28 weeks of age. n = 6 biological replicates. Significance was tested with a one-way ANOVA with Tukey's multiple comparisons test. P-values are * < 0.05, ** < 0.01, *** < 0.001, **** < 0.0001.

https://doi.org/10.1038/s44161-026-00818-2

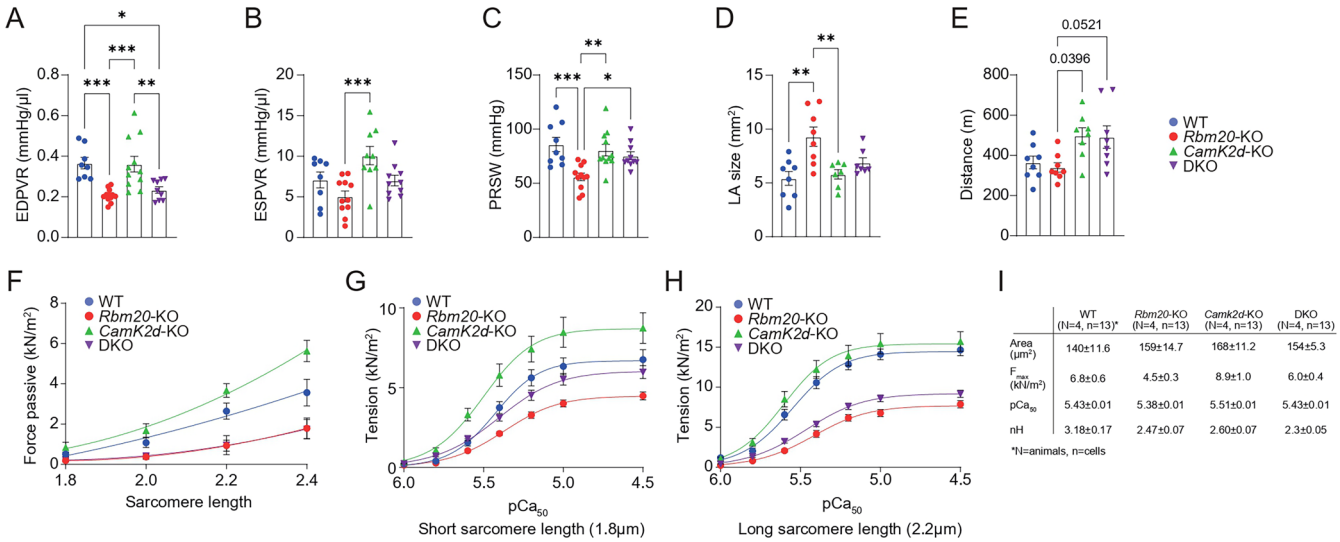

	WT (N=4, n=13)*	*Rbm20*-KO (N=4, n=13)	*Camk2d*-KO (N=4, n=13)	DKO (N=4, n=13)
Area (µm²)	140±11.6	159±14.7	168±11.2	154±5.3
F_{max} (kN/m²)	6.8±0.6	4.5±0.3	8.9±1.0	6.0±0.4
pCa_{50}	5.43±0.01	5.38±0.01	5.51±0.01	5.43±0.01
nH	3.18±0.17	2.47±0.07	2.60±0.07	2.3±0.05

*N=animals, n=cells

Extended Data Fig. 3 | Functional measurements of *Rbm20/Camk2d* DKO mouse hearts/cardiomyocytes. a. End-diastolic pressure volume relationship measured by PV-loops (n = 8 biological replicates for WT, n = 12 biological replicates for *Rbm20*-KO, n = 11 biological replicates for *Camk2d*-KO, and n = 9 biological replicates for DKO). Significance was tested with a one-way ANOVA with Tukey's multiple comparisons test. P-values are * < 0.05, ** < 0.01, *** < 0.001. **b**. End-systolic pressure volume relationship measured by PV-loops. (n = 8 biological replicates for WT, n = 11 biological replicates for *Rbm20*-KO, n = 9 biological replicates for *Camk2d*-KO, and n = 10 biological replicates for DKO) **c**. Preload-recruitable stroke work measured by PV-loops (n = 9 biological replicates for WT, n = 11 biological replicates for *Rbm20*-KO, n = 11 biological replicates for *Camk2d*-KO, and n = 10 biological replicates for DKO). **d**. Atrial size at 12 weeks of age measured by atrial echocardiography (n = 8 biological replicates for WT and *Rbm20*-KO, n = 7 biological replicates for *Camk2d*-KO and DKO). **e**. Exercise tolerance test (n = 8 biological replicates). **f**. Passive force development of skinned cardiomyocytes. (N = 4 and n = 11 replicates for WT, N = 4 and n = 12 replicates for *Rbm20*-KO, N = 4 and n = 18 replicates for *Camk2d*-KO, and N = 4 and n = 22 replicates for DKO, where N=animals and n=cells). **g-h**. Tension-Ca^{2+} relation at short (1.8 µm) and long (2.2 µm) sarcomere length. (N = 4 and n = 11 replicates for WT, N = 4 and n = 12 replicates for *Rbm20*-KO, N = 4 and n = 19 replicates for *Camk2d*-KO, and N = 4 and n = 21 replicates for DKO, where N=animals and n=cells). **i**. Values of isometric force development at sarcomere length of 1.8 µm.

https://doi.org/10.1038/s44161-026-00818-2

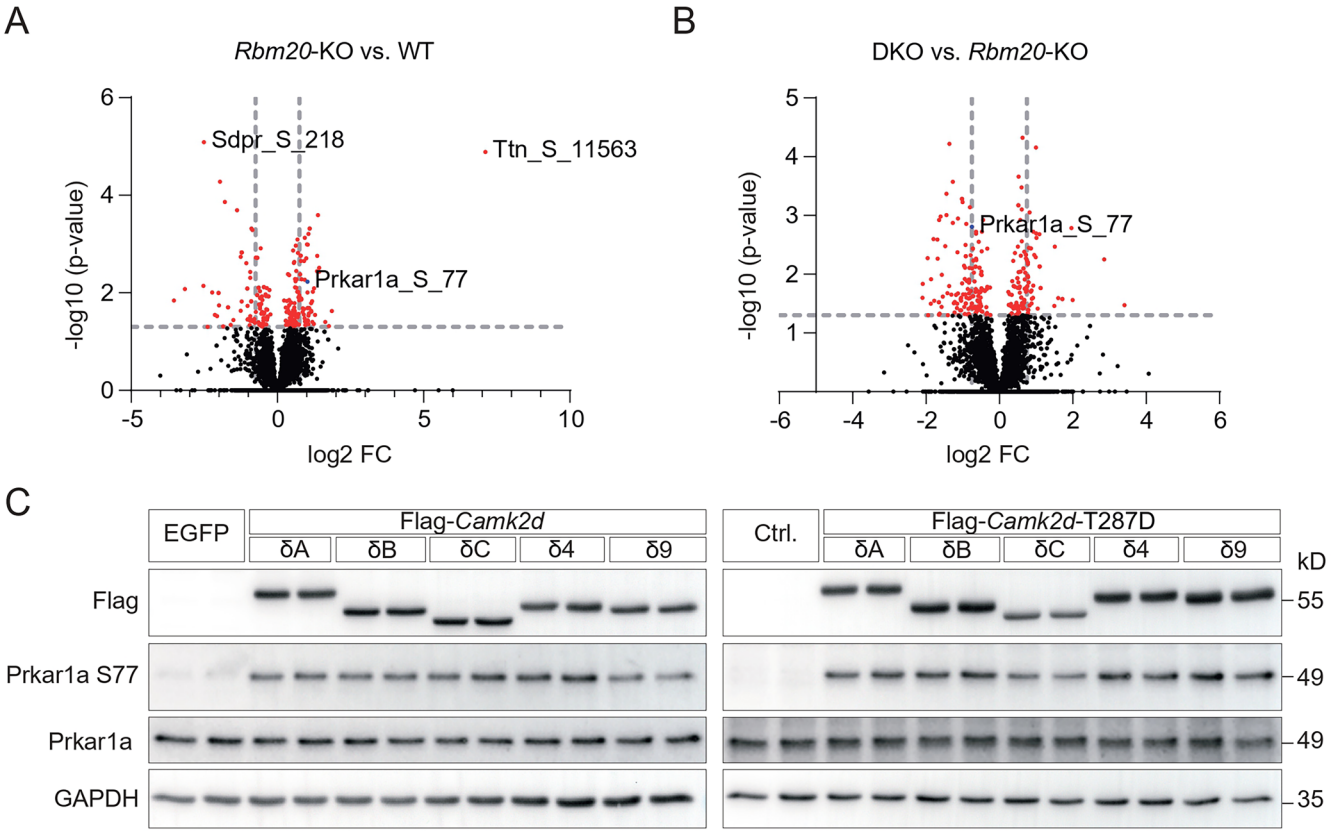

Extended Data Fig. 4 | Phosphoproteomics of *Rbm20/Camk2d* DKO mouse hearts. a. Volcano plot of differentially phosphorylated proteins in the hearts of *Rbm20* KO mice. **b.** Volcano plot of differentially phosphorylated proteins in the hearts of DKO vs. *Rbm20* KO mice. **c.** Overexpression of WT and constitutively active (T287D) CAMK2D splice variants in HEK293 cells is sufficient to induce PRKAR1A phosphorylation at Serine 77.

https://doi.org/10.1038/s44161-026-00818-2

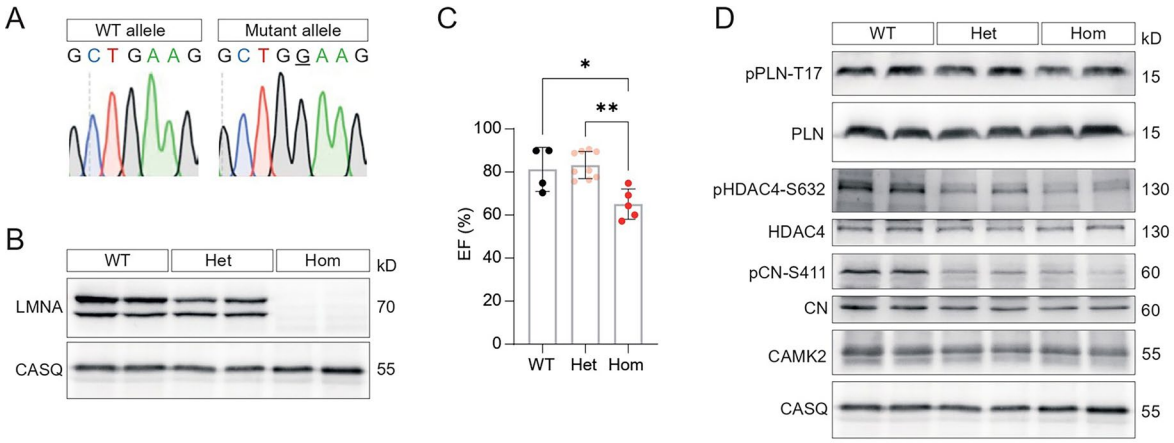

Extended Data Fig. 5 | Mouse model with LMNA-K117fs mutation. a. Sanger sequencing of wildtype and mutant LMNA allele. **b**. Western blot of LMNA in wildtype, heterozygous, and homozygous LMNA-K117fs mouse hearts. (n = 4 biological replicates for WT, n = 9 biological replicates for Het, and n = 5 biological replicates for Hom). **c**. Ejection fraction at 3 weeks of age. Significance was tested with a one-way ANOVA with Tukey's multiple comparisons test. P-values are * < 0.05, ** < 0.01. **d**. Western blots of CAMK2D phosphorylation targets.

https://doi.org/10.1038/s44161-026-00818-2

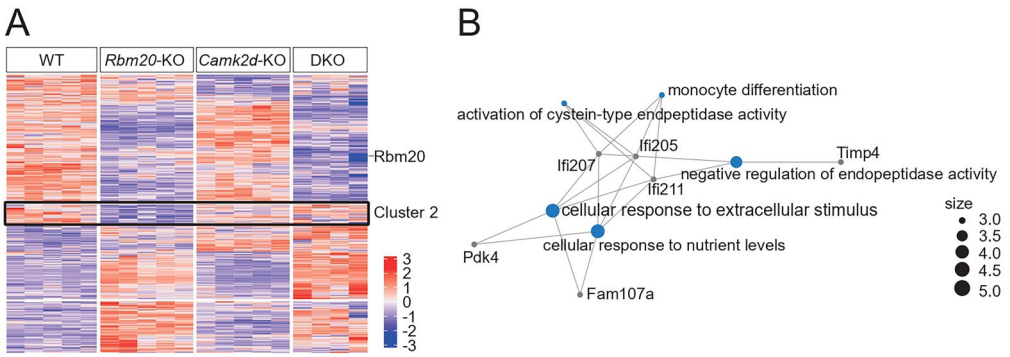

Extended Data Fig. 6 | Transcriptomic analysis of *Rbm20/Camk2d* DKO mouse hearts. a. Heatmap of DEGs in the hearts of WT, *Rbm20* KO, *Camk2d* KO, and *Rbm20/Camk2d* DKO mice. **b.** Gene set enrichment analysis of cluster 2.

https://doi.org/10.1038/s44161-026-00818-2

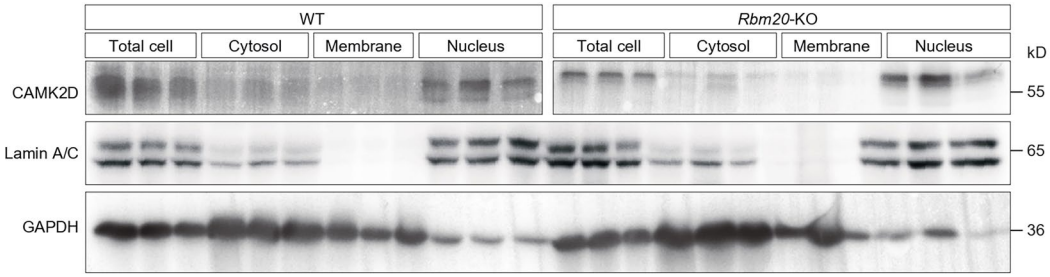

Extended Data Fig. 7 | Fractionation of left ventricular tissue of WT and *Rbm20* KO mice. Cellular fractionation of left ventricular tissue of WT and *Rbm20* KO mouse hearts. Lamin A/C denotes the nuclear fraction, while GAPDH denotes the cytoplasmic fraction.

https://doi.org/10.1038/s44161-026-00818-2

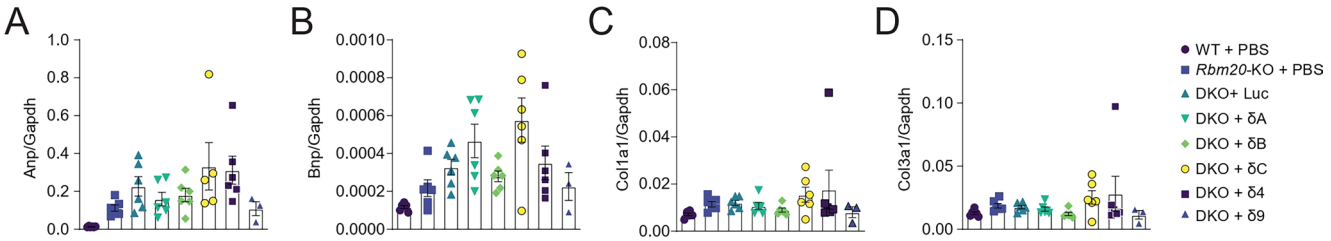

Extended Data Fig. 8 | Expression of marker genes in DKO mouse hearts with re-expression of CAMK2D. a-d. qPCR analysis of *Anp* (*Anf*), *Bnp*, *Col1a1*, and *Col3a1* in the hearts of DKO mice after re-expression of single cardiac CAMK2D splice variants (n = 6 biological replicates, except DKO + δA (n = 5) and DKO + δ9 (n = 3)).

https://doi.org/10.1038/s44161-026-00818-2

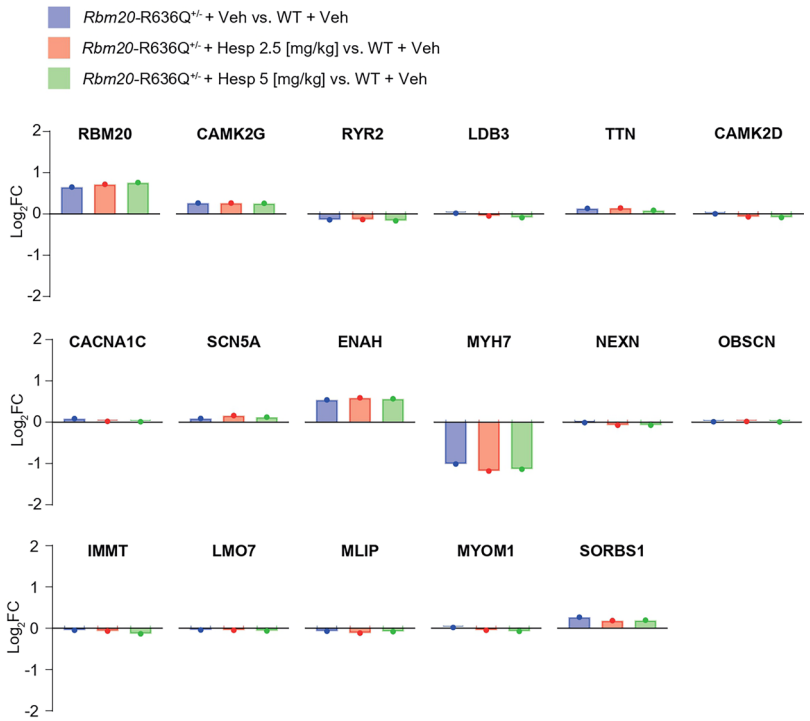

Extended Data Fig. 9 | Hesperadin treatment does not affect protein expression of RBM20 or RBM20 splicing targets. Log2FC of protein expression from proteomic data of *Rbm20*-R636Q$^{+/-}$ mouse hearts with vehicle treatment (blue bars), with 2.5 µg/kg hesperadin treatment (red bars), or with 5 µg/kg hesperadin treatment (green bars) versus wildtype mouse hearts with vehicle treatment.

https://doi.org/10.1038/s44161-026-00818-2

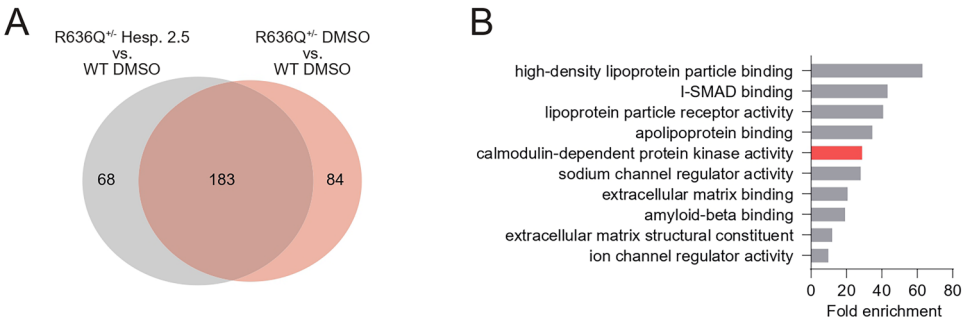

Extended Data Fig. 10 | Hesperadin treatment inhibits CAMK2D activity in *Rbm20*-R636Q KI mice. a. Venn Diagram of upregulated genes in vehicle and hesperadin (2.5 µg/kg) treated heterozygous *Rbm20*-R636Q KI mouse hearts. **b.** Gene ontology enrichment analysis of genes uniquely upregulated in vehicle treated heterozygous *Rbm20*-R636Q KI mouse hearts.

nature portfolio

Corresponding author(s): M. van den Hoogenhof
J.backs

Last updated by author(s): Dec 12, 2025

Reporting Summary

Nature Portfolio wishes to improve the reproducibility of the work that we publish. This form provides structure for consistency and transparency in reporting. For further information on Nature Portfolio policies, see our Editorial Policies and the Editorial Policy Checklist.

Statistics

For all statistical analyses, confirm that the following items are present in the figure legend, table legend, main text, or Methods section.

n/a	Confirmed	
☐	☒	The exact sample size (*n*) for each experimental group/condition, given as a discrete number and unit of measurement
☐	☒	A statement on whether measurements were taken from distinct samples or whether the same sample was measured repeatedly
☐	☒	The statistical test(s) used AND whether they are one- or two-sided *Only common tests should be described solely by name; describe more complex techniques in the Methods section.*
☒	☐	A description of all covariates tested
☐	☒	A description of any assumptions or corrections, such as tests of normality and adjustment for multiple comparisons
☐	☒	A full description of the statistical parameters including central tendency (e.g. means) or other basic estimates (e.g. regression coefficient) AND variation (e.g. standard deviation) or associated estimates of uncertainty (e.g. confidence intervals)
☐	☒	For null hypothesis testing, the test statistic (e.g. *F*, *t*, *r*) with confidence intervals, effect sizes, degrees of freedom and *P* value noted *Give P values as exact values whenever suitable.*
☒	☐	For Bayesian analysis, information on the choice of priors and Markov chain Monte Carlo settings
☒	☐	For hierarchical and complex designs, identification of the appropriate level for tests and full reporting of outcomes
☒	☐	Estimates of effect sizes (e.g. Cohen's *d*, Pearson's *r*), indicating how they were calculated

Our web collection on statistics for biologists contains articles on many of the points above.

Software and code

Policy information about availability of computer code

Data collection	Leica LAS X software was used in the acquisition of confocal imaging and histological staining (bright-field) data (Leica Mica).
Data analysis	Echocardiography: VevoLab software version 5.8.2 (Visual Sonics). RNAseq analysis: R (4.2.3), Rsubread R package, FastQC, Trimmomatic, BiocManager, ShortRead, DESeq2 (1.38.3), ClusterProfiler (4.4.4), Regtools (1.0.0), ComplexHeatmap (2.12.1).

For manuscripts utilizing custom algorithms or software that are central to the research but not yet described in published literature, software must be made available to editors and reviewers. We strongly encourage code deposition in a community repository (e.g. GitHub). See the Nature Portfolio guidelines for submitting code & software for further information.

Data

Policy information about availability of data

All manuscripts must include a data availability statement. This statement should provide the following information, where applicable:

- Accession codes, unique identifiers, or web links for publicly available datasets
- A description of any restrictions on data availability
- For clinical datasets or third party data, please ensure that the statement adheres to our policy

All RNA-sequencing data has been deposited at GEO under the accession number GSE311410.

Research involving human participants, their data, or biological material

Policy information about studies with human participants or human data. See also policy information about sex, gender (identity/presentation), and sexual orientation and race, ethnicity and racism.

Reporting on sex and gender	*Use the terms sex (biological attribute) and gender (shaped by social and cultural circumstances) carefully in order to avoid confusing both terms. Indicate if findings apply to only one sex or gender; describe whether sex and gender were considered in study design; whether sex and/or gender was determined based on self-reporting or assigned and methods used.* *Provide in the source data disaggregated sex and gender data, where this information has been collected, and if consent has been obtained for sharing of individual-level data; provide overall numbers in this Reporting Summary. Please state if this information has not been collected.* *Report sex- and gender-based analyses where performed, justify reasons for lack of sex- and gender-based analysis.*
Reporting on race, ethnicity, or other socially relevant groupings	*Please specify the socially constructed or socially relevant categorization variable(s) used in your manuscript and explain why they were used. Please note that such variables should not be used as proxies for other socially constructed/relevant variables (for example, race or ethnicity should not be used as a proxy for socioeconomic status).* *Provide clear definitions of the relevant terms used, how they were provided (by the participants/respondents, the researchers, or third parties), and the method(s) used to classify people into the different categories (e.g. self-report, census or administrative data, social media data, etc.)* *Please provide details about how you controlled for confounding variables in your analyses.*
Population characteristics	*Describe the covariate-relevant population characteristics of the human research participants (e.g. age, genotypic information, past and current diagnosis and treatment categories). If you filled out the behavioural & social sciences study design questions and have nothing to add here, write "See above."*
Recruitment	*Describe how participants were recruited. Outline any potential self-selection bias or other biases that may be present and how these are likely to impact results.*
Ethics oversight	*Identify the organization(s) that approved the study protocol.*

Note that full information on the approval of the study protocol must also be provided in the manuscript.

Field-specific reporting

Please select the one below that is the best fit for your research. If you are not sure, read the appropriate sections before making your selection.

☒ Life sciences ☐ Behavioural & social sciences ☐ Ecological, evolutionary & environmental sciences

For a reference copy of the document with all sections, see nature.com/documents/nr-reporting-summary-flat.pdf

Life sciences study design

All studies must disclose on these points even when the disclosure is negative.

Sample size	Sample sizes were determined based on similar studies in our field.
Data exclusions	1 sample (out of 5) of the DKO group in the RNAseq from Supp. Figure 4 was excluded, as it was an outlier in all genes measured. No other exclusions.
Replication	Experiments were performed in at least 3 independent biological replicates, with the exception of the animal experiments with AAV-injections and Hesperadin treatment (due to ethical restraints). All attempts at replication were succesfull.
Randomization	Organisms for all phenotypic characterizations were randomly chosen among each genotype population.
Blinding	Investigators were blinded during data analysis.

Reporting for specific materials, systems and methods

We require information from authors about some types of materials, experimental systems and methods used in many studies. Here, indicate whether each material, system or method listed is relevant to your study. If you are not sure if a list item applies to your research, read the appropriate section before selecting a response.

Materials & experimental systems

n/a	Involved in the study
☐	☒ Antibodies
☐	☒ Eukaryotic cell lines
☒	☐ Palaeontology and archaeology
☐	☒ Animals and other organisms
☒	☐ Clinical data
☒	☐ Dual use research of concern
☒	☐ Plants

Methods

n/a	Involved in the study
☒	☐ ChIP-seq
☒	☐ Flow cytometry
☒	☐ MRI-based neuroimaging

Antibodies

Antibodies used

1. anti-CAMK2 (611293, BD Biosciences)
2. anti-GAPDH (MAB374, Sigma)
3. anti-Flag (F1804, Sigma)
4. anti-RBM20 (PA5-58068, Thermo Fisher)
5. anti-alpha actinin (A7811, Sigma)

Validation

1. https://www.bdbiosciences.com/en-de/products/reagents/microscopy-imaging-reagents/immunofluorescence-reagents/purified-mouse-anti-cam-kinase-ii.611293?tab=product_details
2. https://www.sigmaaldrich.com/DE/de/product/mm/mab374?srsltid=AfmBOooBqkF0gBrkFEvqFGlOaUd5Ty4Mq_kmaZsqk_znLN-PJexdZXdp
3. https://www.sigmaaldrich.com/DE/de/product/sigma/f1804?utm_source=google&utm_medium=cpc&utm_id=22188460044&utm_campaign=%7Bcampaignname%7D&utm_content=173144970223&utm_term=f1804+sigma&gad_source=1&gad_campaignid=22188460044&gclid=Cj0KCQjwuvrBBhDcARIsAKRrkjde47mnCrepLavbMwe2Iz0B_sG32LpQu8z7XkTdHcoLvKg7tR8XTCMaAoSkEALw_wcB
4. https://www.thermofisher.com/antibody/product/Rbm20-Antibody-Polyclonal/PA5-58068
5. https://www.sigmaaldrich.com/DE/de/product/sigma/a7811?srsltid=AfmBOopWOI39McS-Be2u_tBpQu9vvT2Juakt-dlRlWYunYW1tIlofd1i

Eukaryotic cell lines

Policy information about cell lines and Sex and Gender in Research

Cell line source(s)	HEK293A (ATCC)
Authentication	https://www.atcc.org/products/crl-1573
Mycoplasma contamination	This cell line tested negative for mycoplasma
Commonly misidentified lines (See ICLAC register)	*Name any commonly misidentified cell lines used in the study and provide a rationale for their use.*

Animals and other research organisms

Policy information about studies involving animals; ARRIVE guidelines recommended for reporting animal research, and Sex and Gender in Research

Laboratory animals	Wildtype, Rbm20 KO, Camk2d KO, and DKO had a mixed FVB and C57/Bl6n background. Rbm20-R636Q mice and LMNAfs-K117 mice had a C57BL/6j background.
Wild animals	This study did not involve wild animals.
Reporting on sex	Both male and female mice were used in this study. Previous studies confirmed there was no sex difference in the strains used, and analysis of data separated by sex did not reveal differences between males and females.
Field-collected samples	This study did not involve field-collected samples.
Ethics oversight	This study adheres to the EU Directive (2010/63/EU) and received approval from the Institutional Animal Care and Use Committee at the Regierungspräsidium Karlsruhe, Germany (approval numbers G120-17, G233/17, and G225/20).

Note that full information on the approval of the study protocol must also be provided in the manuscript.

Plants

Seed stocks

Report on the source of all seed stocks or other plant material used. If applicable, state the seed stock centre and catalogue number. If plant specimens were collected from the field, describe the collection location, date and sampling procedures.

Novel plant genotypes

Describe the methods by which all novel plant genotypes were produced. This includes those generated by transgenic approaches, gene editing, chemical/radiation-based mutagenesis and hybridization. For transgenic lines, describe the transformation method, the number of independent lines analyzed and the generation upon which experiments were performed. For gene-edited lines, describe the editor used, the endogenous sequence targeted for editing, the targeting guide RNA sequence (if applicable) and how the editor was applied.

Authentication

Describe any authentication procedures for each seed stock used or novel genotype generated. Describe any experiments used to assess the effect of a mutation and, where applicable, how potential secondary effects (e.g. second site T-DNA insertions, mosiacism, off-target gene editing) were examined.